The International Journal of Advanced Manufacturing Technology (2022) 118:1141–1163
https://doi.org/10.1007/s00170-021-07885-8

ORIGINAL ARTICLE

Understanding the surface integrity of laser surface engineered tungsten carbide

Kafayat Eniola Hazzan[1] · Manuela Pacella[1] · Tian Long See[2]

Received: 15 April 2021 / Accepted: 15 August 2021 / Published online: 14 September 2021

Abstract

The study investigated the effect of fibre laser processing (1060 nm, 240-ns pulse duration) on the surface integrity of tungsten carbide (WC). The induced surface damage ranged from crack formation, porosity, balling, to spherical pores; the severity and presence of each were dependent on the laser parameters selected. The influence of fluence (0.05–0.20 J/cm^2), frequency (5–100 kHz), feed speed (250–2500 mm/s) and hatch distance (0.02–0.06 mm) on 2D and 3D surface roughness were analysed using the Taguchi technique. Fluence, frequency, and the interaction effect of these were the most influential factors on the surface integrity; from this a linear model was generated to predict the surface roughness. The model performed best at moderate to medium level of processing with an error between 1 and 10 %. The model failed to predict the material response as accurately at higher fluences with percentage errors between 15 and 36 %. In this study, a crack classification system and crack density variable were introduced to estimate the number of cracks and crack type within a 1-mm^2 area size. Statistical analysis of variance (ANOVA) found that fluence (63.49%) and frequency (29.38%) had a significant effect on the crack density independently but not the interaction of both. The crack density was minimised at 0.149 J/cm^2 and 52.5 kHz. To the author's knowledge, for the first time, a quantitative analysis of the crack formation mechanism for brittle materials is proposed (post laser processing).

Keywords Tungsten carbide · Laser processing · Surface optimisation · Laser modelling · Surface integrity · Crack formation

1 Introduction

Tungsten carbide (WC) is a hard ceramic composite metal, with a polycrystalline microstructure, the binder used in sintering adds toughness properties to offset the brittle nature of the ceramic. It is the most widely utilised cutting tool material in a range of applications: turning, milling, high-speed cutting and high-value manufacturing [1]. The unique characteristic of having both metallic and ceramic properties gives WC high strength, durability and the ability to withstand high temperatures [2].

Cutting tools need to be manufactured to small tolerances to produce the desired geometry or features on a workpiece surface. Laser machining is a precise and non-contact operation for processing cutting tools [3], however, the process can induce both mechanical and thermal defects. In WC these microstructural defects are mainly cracking, thermal shock [4], porosity [5], recast layer and heat-affected zone (HAZ) [1]. These defects limit the tool performance and life [2] and act as stress raisers and points of crack initiation, as cutting tools are subjected to large loads and forces.

Cracks are narrow ruptures; the size and depth indicate the amount of damage caused. During laser processing, material phases undergo thermal expansion, expanding during the heating phase and contracting during the cooling/resolidification stage [6]. If there is a significant difference in the expansion rates, a thermal mismatch will occur leading to micro-cracks [7]. If this occurs in an uncontrolled manner across the microstructure, this leads to thermal shock, this is particularly of concern with composite materials like WC with a cobalt binder ([8, 9]). The characteristics of cracks are also defined by their specific location within a microstructure. In polycrystalline materials, these are commonly boundary cracks which run between element grains ([10, 11]), intergranular cracks ([11, 12]) which run within material phases

✉ Manuela Pacella
M.Pacella@lboro.ac.uk

[1] Wolfson School of Mechanical, Electrical and Manufacturing Engineering, Loughborough University, Loughborough, Leicestershire LE11 3TU, UK

[2] The Manufacturing Technology Centre (MTC) Ltd., Pilot Way, Ansty Park, Coventry CV7 9JU, UK

and radial cracks ([13]) which are located between the substructure of the processing area. Mao et al. [14] induced these types of cracks when changing the laser parameters to cut cBN-WC-10Co composites. At high-energy settings, there was a reduction in cracks but the processed material showed other thermal defects like HAZ.

Current methods in choosing the right parameters to minimise processing defects rely on human judgement or selectively testing possible settings and determining the right combination which gives the desired result. Marimuthu et al. [1] used a picosecond laser to machine WC; increasing the laser fluence between 1.27 and 17.3 J/cm^2 increased the ablation depth and surface roughness of the achieved grooves. A simultaneous increase of frequency and speed created a better quality with no significant thermal defects, e.g. recast layer, micro-cracks and HAZ. The study also determined that the material removal rate was proportional to the average laser power. Similarly, Dumitru et al. [15] found that increasing the fluence from 0.4 to 2.8 J/cm^2 caused a higher surface roughness with large pores in the processing crater and physical damage on the surface when processing various ultrahard materials with a femtosecond laser.

Recently, various statistical and analytical techniques, e.g. regression, orthogonal arrays, Taguchi design of experiments (DOE) and analysis of variance (ANOVA), are used to compare the effects parameters have on the operation output and statistically examine the significance of each parameter [16]. They are simple tools to understand multi-variate behaviour compared to finite element approaches which require high computational input and expertise. Ayyildiz et al. [17] used Taguchi experiment design for surface roughness optimisation in the drilling of fibreboard and ANOVA for experimental analysis to find the optimal roughness. The statistical approach also determined that the parameters followed a quadratic regression rather than a linear regression for roughness optimisation. Kara et al. [18] also demonstrated the use of Taguchi for grinding optimisation on AISI 5140 and compare linear and quadratic correlation to surface roughness with a high success. In laser processing, statistical optimisation has been conducted on hard and ultra-hard materials ([19–21]). For example, Wang et al. [22] used DOE to optimise a hybrid laser waterjet on polycrystalline cubic boron nitride (PcBN); laser power and waterjet pressure were the most significant factors on the cut quality. Altering these parameters improved the cut quality reducing taper size and HAZ thereby controlling phase transitions in the microstructure. Calderón Urbina et al. [23] conducted an analytical investigation into the material removal rate of laser ablation on WC. Laser power, burst-mode pulse overlaps and scanning pattern were the factors of interest. It concluded that the laser power and overlap were the most influential variables on the ablation process.

Previous research shows that even simple modelling provides an objective and reproducible methodology to understand processing and material behaviour. However, fewer works have reported the optimisation of laser parameters for brittle materials (i.e., WC) based on crack formation and surface integrity. In cutting tools, cracking is a type of surface defect that strongly hinders tool performance; therefore, optimising and controlling the laser process to avoid crack formation are needed as studies have done in other materials [24].

1.1 Scope of the paper

Laser manufacturing of WC requires a thorough understanding of WC behaviour to improve the quality of the process and ensure that the resultant microstructure does not have an adverse effect on the cutting tool performance. WC is inherently brittle and falls under the group of materials that will fracture under thermal effects. The cemented carbides' response to mechanical and electrical processes, e.g. grinding, turning, electrical discharge machining (EDM) and electrochemical machining (ECM), has been greatly reviewed, but limited research is reported on WC response to laser beam processes, i.e. heating and melting. The objectives of the research paper are:

- To experimentally investigate the effect of laser parameters on the surface morphology and integrity on a WC cutting tool material using a pulsed fibre laser (1060-nm wavelength, 70-W maximum output power). The parameters chosen were fluence, frequency, feed speed and hatch distance.
- Generate a numerical linear model to predict the surface roughness in relation to the distribution of surface peaks generated by laser processing, using DOE optimisation techniques.
- To investigate the crack formation and fracture behaviour of WC using ANOVA by developing a new method for classifying surface cracks produced from laser processing. This includes the analysis of surface crack generation based on the most influential factors to the surface roughness.

2 Methodology

2.1 Workpiece material

The study used a WC-Co12 % blank (Ultra-met Z57 corresponding to an industrial grade C5 ANSI standard, P50 ISO Grade) with a mean grain size of 4 μm and 1.60-mm thickness on a molybdenum carbide substrate. This grade is typically used in turning and milling on softer alloyed materials at medium speeds [2]. The chemical composition of the

sample, measured by energy-dispersive spectroscopy (EDS), is given in Table 1.

2.2 Laser machining

A 70-W InnoLas micro-machining system (MMS) fibre laser 1060 nm was used, with a beam mode profile of $M^2 < 1.6$; set up shown in Figure 1a. The laser is equipped with pre-programmed waveforms. Waveform 0 was used as a default setting: pulse duration of 240 ns, max pulse energy 1 mJ; this gives a maximum fluence of 0.20 J/cm^2. This is lower than the WC ablation threshold of 0.45 J/cm^2 in the ns regime [15]; thus, laser mechanism discussed in this paper focused on melting and partial ablation of the binder. The beam diameter at the focal height of 60.5 mm was 80 μm; the generated laser fluences were calculated based on previous research from Pacella et al. [25]. A 1-mm^2 square was processed for each experiment using one pass in a path pattern as shown in Figure 1b.

2.2.1 Experiment design

A 2^4 factorial design consisted of four factors (fluence, frequency, speed and hatch distance) with two levels, giving 16 experimental conditions, repeated three times. All other laser parameters and conditions were kept constant, including the number of scan repetitions and laser spot size. Table 2 and Table 3 outline the parameter settings for each experiment. A reference experiment was also conducted between the two levels of each factor. The low and high levels of hatch distances and feed speed give an overlap of 83% and 50% respectively, calculated based on previous research by Dahotore and Marimkar [26]. The selection of laser parameters was based on the settings available on the InnoLas MMS and common laser parameters used to process WC ([15, 27–29]).

The DOE experiment also acted as a screening test to identify the main parameters affecting the microstructure and surface integrity, leading to further experiments, discussed in this section. The second set of experiment (Table 4) focused on understanding the material response to irradiance with fluence and frequency (v = 500 mm/s, d = 0.02 mm), with parameter values distributed between the minimum and maximum settings of the InnoLas MMS to highlight the micro-crack generation, crack density and microstructural characteristics. An orthogonal array of 49 experiments was made with 7 settings for both factors; it was repeated three times to increase robustness; using an orthogonal array reduced the number of experiments needed. ANOVA was applied to experimental results to identify the variation caused by changing process parameters on crack formation and crack density. It was also utilised to find the significance and impact of parameters on crack density.

The feed speed was also investigated independently to understand other material phenomenon, with 6 experiments varied between 250 and 2500 mm/s (ψ = 0.050 J/cm^2, f = 52.5 kHz, d = 0.02 mm), repeated three times (orthogonal array).

Table 1 Chemical weight percentage composition of unprocessed WC-Co12 % disk

Element	W	C	Co	O	Al	Fe	Si
wt%	41.6	24.0	12.4	15.8	2.2	2.2	1.8

2.3 Characterisation

Post laser processing, the samples were cleaned with an acetone solution to remove dirt and debris prior to characterisation. The surface roughness and 3D profile were measured using an Alicona Infinite Focus White light interferometry (WLI) and analysed using MountainLab software. A lateral resolution of 3 μm and vertical resolution of 50 nm were utilised. The surface was levelled to remove tilt, and waviness removed with a Robust Gaussian Filter and 0.25-mm cut-off. Three roughness Ra measurements were taken vertically and horizontally for each sample and averaged. The vertical and horizontal surface roughness were separate to isolate specific details of the laser process. The horizontal roughness (RaH) captured detail on the surface along the laser path. The vertical roughness (RaV) captured detail through laser passes (Figure 1c). Various 3D roughness measurements were taken using Abbott-Firestone's curve, but the reduced peak height (Spk) was the measure of concern also known as the peak distribution on the surface. A high Spk implies that the surface has many peaks. The initial contact with another surface will cause most of the forces to be confined to these small peaks, thus increasing the contact pressure. This leads to surfaces quickly eroding and being worn down, a necessary consideration in cutting tools. This variable is also useful to know for the amount of area for lubricant retention and debris collection available. Scanning electron microscope (SEM), TM3030 Hitachi backscatter SEM, was used to view the surface topography in particular to identify microstructure defects such as cracks, thermal shock, voids, pores, splatter and balling as a result of laser processing. These defects affect the performance of a material in application [30]. Energy-dispersive spectroscopy (EDS) analysis for chemical composition was also applied in various regions. The material removal was calculated based on previous research [25].

2.4 Crack analysis

A new method was developed to estimate crack density to characterise crack formation in laser treated specimens. Cracks were identified as regions of material separation

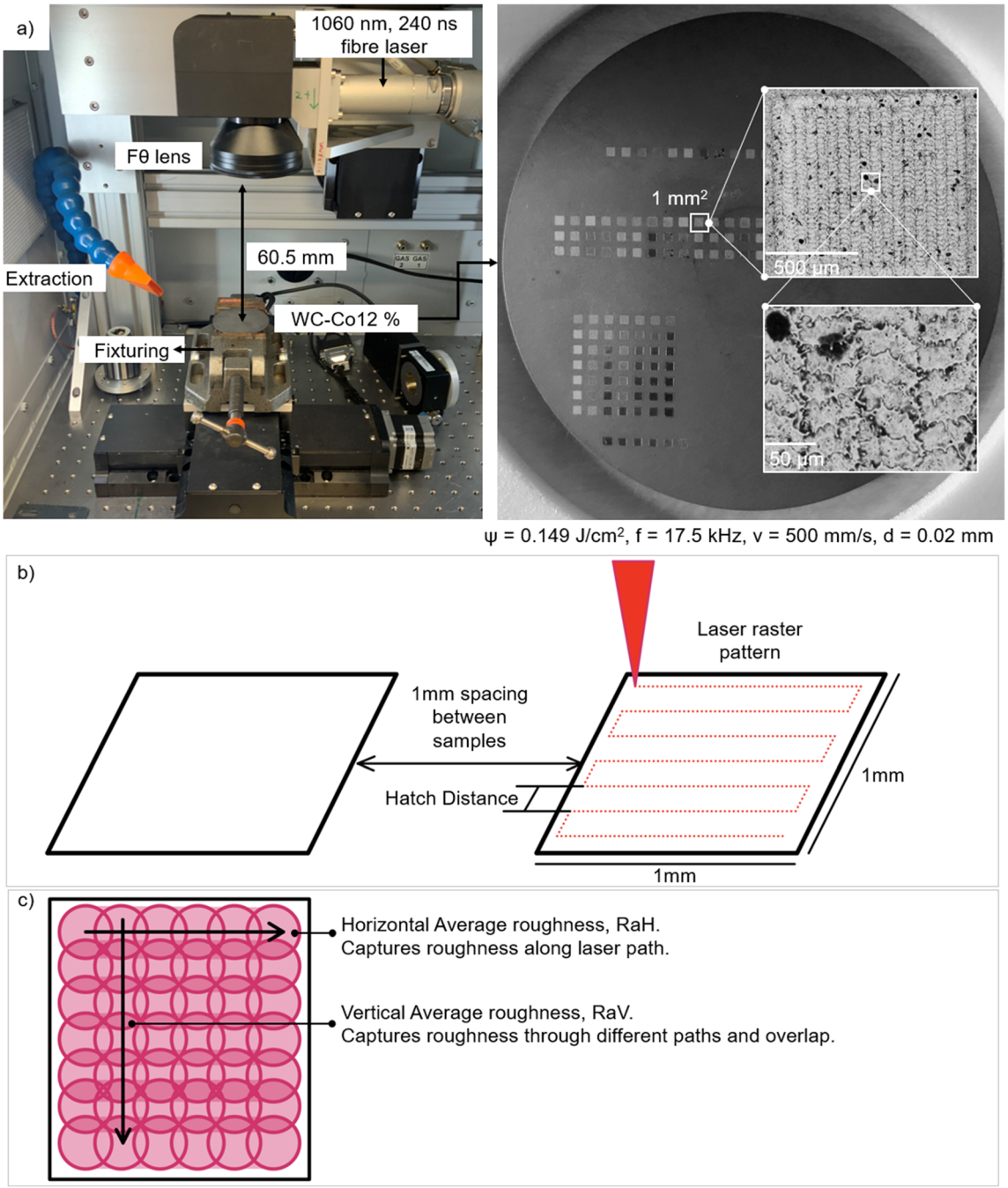

Fig. 1 **a** Experimental set up. **b** Laser raster pattern. **c** 2D average roughness parameters in the vertical and horizontal directions

distinctly different from other surface defects such as a splatter boundary that follows the molten material shape. Firstly, the cracks were classified into three categories based on size: superficial cracks, micro-cracks and deep cracks by SEM inspection of the samples. Superficial cracks were faint, hairline scratches (length up to 20 µm). Micro-cracks were thicker cracks or cracks longer than 20 µm (length up to 100 µm, width up to 3 µm). Deep cracks were cracks that caused significant damage/breakage or void-like failures (or length ≥ 20 µm and width > 3 µm). All the cracks in a 225 µm × 175 µm sample space were outlined, categorised and counted for each sample (Figure 2).

Table 2 DOE experiment levels

Factors of interest	Units	Symbol	Low level (-1)	High level (1)
Fluence	J/cm^2	ψ	0.050	0.149
Repetition frequency	kHz	f	17.5	52.5
Feed speed	mm/s	v	500	1500
Hatch Distance	mm	d	0.02	0.06

Table 3 Taguchi 2^4 orthogonal array factorial design—parameter settings for each experiment

Experiment	ψ	Fluence	f	Frequency	v	Speed	d	Hatch
0	0	0.099	0	35.0	0	1000	0	0.04
1	-1	0.050	-1	17.5	-1	500	-1	0.02
2	1	0.149	-1	17.5	-1	500	-1	0.02
3	-1	0.050	1	52.5	-1	500	-1	0.02
4	-1	0.050	-1	17.5	1	1500	-1	0.02
5	-1	0.050	-1	17.5	-1	500	1	0.06
6	1	0.149	1	52.5	-1	500	-1	0.02
7	1	0.149	-1	17.5	1	1500	-1	0.02
8	1	0.149	-1	17.5	-1	500	1	0.06
9	-1	0.050	1	52.5	1	1500	-1	0.02
10	-1	0.050	1	52.5	-1	500	1	0.06
11	-1	0.050	-1	17.5	1	1500	1	0.06
12	1	0.149	1	52.5	1	1500	-1	0.02
13	-1	0.050	1	52.5	1	1500	1	0.06
14	1	0.149	-1	17.5	1	1500	1	0.06
15	1	0.149	1	52.5	-1	500	1	0.06
16	1	0.149	1	52.5	1	1500	1	0.06

The length and measurement criterion are based on the works of Denkena et al. [31] which studied micro-crack formation in hard metal milling tools. The length of cracks is measured by importing the SEM image into MATLAB and overlaying a straight line from one end to the other. Cracks which deviated from a linear shape were overlayed with several straight lines in segments. The ratio of the workspace compared to the actual SEM size was used to convert the length of the lines drawn to the micron scale. The quantity of each type of crack in the area was scaled up to estimate the crack density present on a 1-mm^2 area, resulting in a crack density value for each type of crack. The crack characterisation extrapolation is a valid estimation as laser processing is well established for its repeatability and reliability [32]. The total number of cracks from each sample was then compared to the fluence and frequency settings used to process that sample, allowing for an ANOVA result to be computed. It was important to generate this technique to have a quantitative analysis of crack formation as there is currently no universal way of quantifying cracks based on type. As this is a visual technique, the sample space used will be dependent on the workpiece material. It should be a size that covers at least three laser paths with the magnification set to view surface cracks to a good resolution. The crack classification is only relevant to surface inspection; the penetration and depth of cracks are out of scope.

Table 4 Experiment number for comparing fluence and frequency for understanding material crack generation (v = 500 mm/s, d = 0.02 mm)

	Experiment number						
Fluence (J/cm^2)	**0.030**	**0.050**	**0.070**	**0.099**	**0.135**	**0.149**	**0.200**
Frequency (kHz)							
5.0	1	8	15	22	29	36	43
17.5	2	9	16	23	30	37	44
28.0	3	10	17	24	31	38	45
40.0	4	11	18	25	32	39	46
52.5	5	12	19	26	33	40	47
75.0	6	13	20	27	34	41	48
100.0	7	14	21	28	35	42	49

3 Results

Surface roughness is a clear way of characterising the surface quality after processing. The as-received sample had an RaH 0.4628 µm, RaV 0.5585 µm and Spk 0.9033 µm. Table 5 shows the roughness values from the experimental data using the corresponding levels described in the 'Experiment design' section. The levels were used to calculate a gradient value respective to each parameter and parameter interactions, calculated using the method described in [33] (Figure 3).

For all three roughness parameters, fluence had the greatest effect. An increase from 0.050 to 0.149 J/cm^2 caused an increase of 0.1203 µm, 0.1644 µm and 0.4189 µm for RaV, RaH and Spk, respectively. For RaV, the interaction of frequency and speed was the next greatest effect. However, speed independently reduced the roughness, but frequency independently increased the roughness. The remaining effects are less contributory. RaH followed a different trend with frequency, the interaction of fluence and frequency and the interaction of fluence, frequency and feed speed cause the most increase in roughness value. Hatch distance had less of an effect suggesting that the energy accumulation from other parameters is more likely to cause a poorer surface than having a smaller pitch between the laser passes.

The factors that consistently reduced the roughness were speed, the interaction between fluence and speed, the interaction between frequency and speed and the interaction of fluence, frequency and feed speed; also confirmed with the lack of defects on the microstructure of certain samples. This suggested that increasing the speed improved 2D and 3D surface roughness, and when optimised with fluence and frequency, an even better result was achieved in terms of 2D and 3D roughness. Table 6 shows the percentage variation of Spk from the as-received surface using Equation (1). Experiments processed at a fluence of 0.050 J/cm^2 had a ± 20% variation from the as-received.

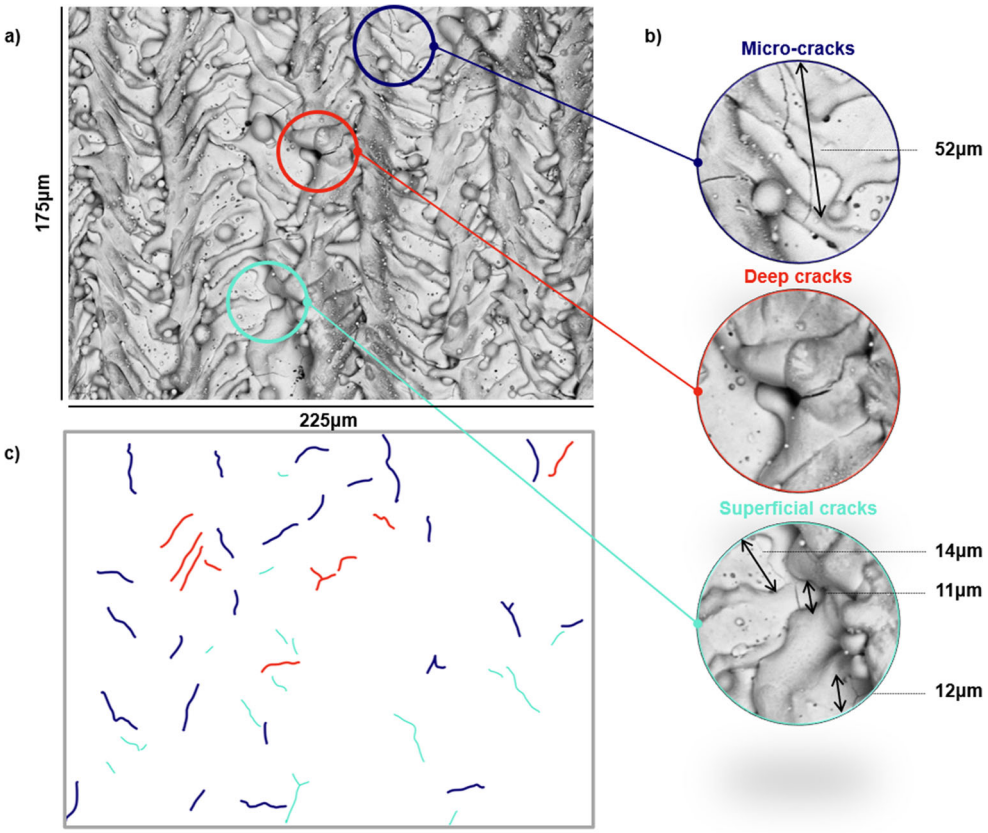

Fig. 2 **a** Example of sample size for crack analysis, **b** examples of crack categorisation based on size and damage to surface, **c** representation of each type of crack from a sample

Table 5 Roughness parameter value for parameters and parameter interaction

Parameter	Effect of	RaV (µm)		RaH (µm)		Spk (µm)	
		-1	1	-1	1	-1	1
ψ	Fluence	0.5607	0.8013	0.5988	0.9276	1.0039	1.8416
f	Frequency	0.5814	0.7806	0.6088	0.9176	1.1688	1.6767
v	Feed speed	0.7655	0.5964	0.8750	0.6514	1.6543	1.1912
d	Hatch distance	0.6430	0.7189	0.6845	0.8419	1.2976	1.5479
ψ*f	Interaction of fluence and frequency	0.6123	0.7496	0.6526	0.8738	1.1752	1.6703
ψ*v	Interaction of fluence and feed speed	0.7503	0.6117	0.8442	0.6822	1.6330	1.2125
ψ*d	Interaction of fluence and hatch distance	0.6175	0.7445	0.7284	0.7980	1.2904	1.5551
f*v	Interaction of frequency and feed speed	0.7946	0.5673	0.8337	0.6927	1.6796	1.1659
f*d	Interaction of frequency and hatch distance	0.6447	0.7173	0.7082	0.8182	1.2588	1.5868
v*d	Interaction of feed speed and hatch distance	0.6973	0.6646	0.8086	0.7178	1.5791	1.2664
ψ*f*v	Interaction of fluence, frequency and feed speed	0.7530	0.6089	0.8624	0.6641	1.7248	1.1207
ψ*f*d	Interaction of fluence, frequency and hatch distance	0.6923	0.6696	0.7583	0.7681	1.2647	1.5808
ψ*v*d	Interaction of fluence, feed speed and hatch distance	0.6832	0.6788	0.7943	0.7321	1.5538	1.2918
f*v*d	Interaction of frequency, feed speed and hatch distance	0.6792	0.6828	0.8074	0.7190	1.6053	1.2402
ψ*f*v*d	Interaction of fluence, frequency, feed speed and hatch distance	0.6953	0.6666	0.7997	0.7267	1.5456	1.2999

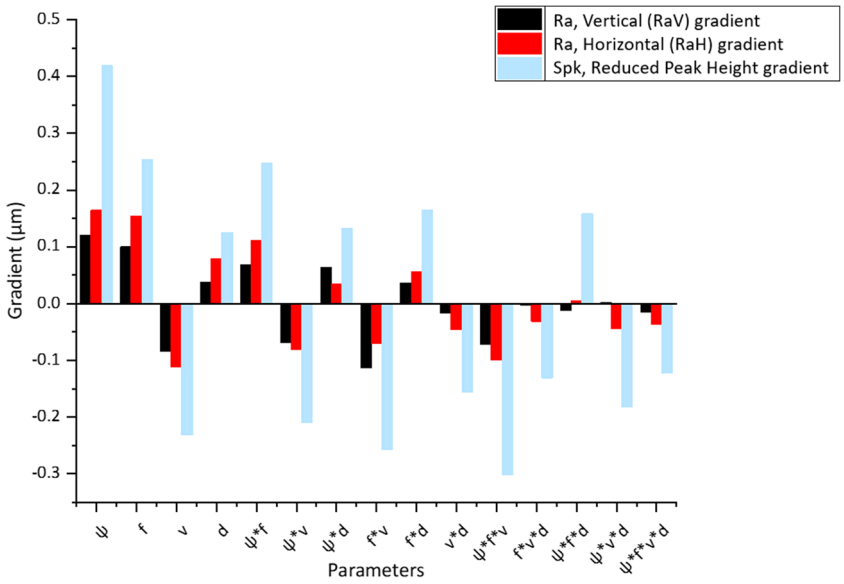

Fig. 3 Gradient values of moving from each level for each parameter

$$\text{Percentage variation } (\%) = \left(\frac{(Spk \text{ value from test}) - (As\text{-received } Spk)}{As\text{-received } Spk}\right) x100 \quad (1)$$

The distribution of the Spk values based on individual parameters is shown in Figure 4. The distribution of Spk values was very small when using the lower fluence compared to the higher fluence setting; the mean is 43% higher. Frequency followed a similar pattern where the lower setting had a much smaller distribution than the higher setting; and a 30 % increase in mean. The speed and hatch distance had a smaller difference, with the quartiles of the roughness values overlapping at the two levels. However, at a higher speed setting, the deviation was within a 10% variation of the as-received Spk value. Hatch distance had the least variational difference between the levels.

Pareto analysis or cumulative frequency (Figure 5) was also conducted on the parameters and the interaction using absolute gradient values, to prioritise which parameters caused a greater change in roughness. Fluence had the highest contributory effect on all roughness variables; in other words, increasing the fluence is more likely to cause a higher surface

Table 6 Percentage variation of Spk form the as-received sample compared to each experiment

Experiment	ψ (J/cm^2)	f (kHz)	v (mm/s)	d (mm)	Percentage variation from as-received surface
0	0.099	35.0	1000	0.04	32%
1	0.050	17.5	500	0.02	23%
2	0.149	17.5	500	0.02	33%
3	0.050	52.5	500	0.02	11%
4	0.050	17.5	1500	0.02	1%
5	0.050	17.5	500	0.06	12%
6	0.149	52.5	500	0.02	140%
7	0.149	17.5	1500	0.02	78%
8	0.149	17.5	500	0.06	38%
9	0.050	52.5	1500	0.02	13%
10	0.050	52.5	500	0.06	7%
11	0.050	17.5	1500	0.06	5%
12	0.149	52.5	1500	0.02	50%
13	0.050	52.5	1500	0.06	16%
14	0.149	17.5	1500	0.06	45%
15	0.149	52.5	500	0.06	400%
16	0.149	52.5	1500	0.06	47%

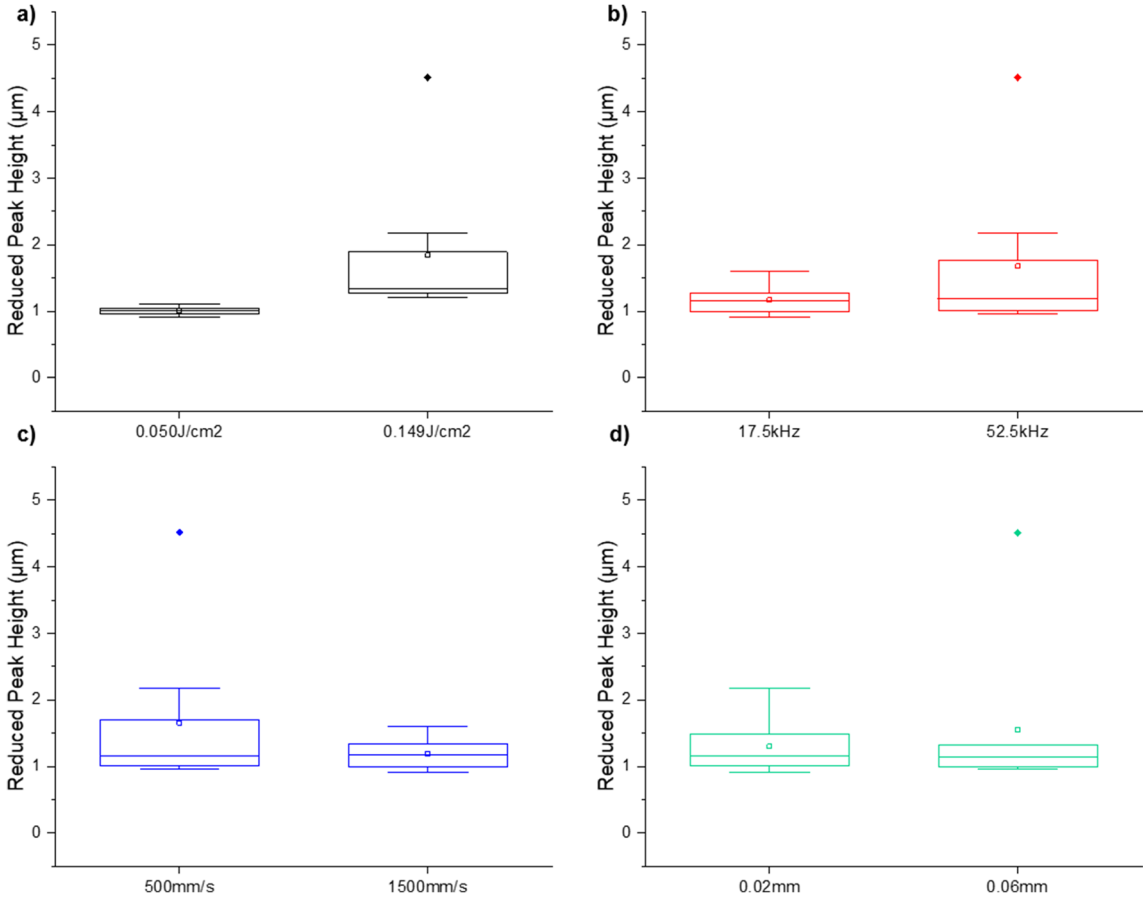

Fig. 4 Box plot of Spk for **a** fluence, **b** frequency, **c** speed and **d** hatch distance

roughness due to the more aggressive material processing irrespective of other laser parameters (see the 'Discussion' section). Therefore, it is a necessary factor to reduce the roughness and have a better surface homogeneity. In all roughness parameters, a variant of frequency and speed (or interaction) had the second greatest effect on the roughness, indicating that speed and frequency need to be viewed as linked parameters when considering surface roughness in both 2D and 3D parameters. Spk was affected by the interactive effects of parameters more where the interaction between fluence, speed and frequency and the interaction of frequency and speed had the next largest contribution to the Spk. This suggested the importance of considering parameters as related variables and not isolated.

Figure 6 shows the main effects plot with the mean Spk value graphically; the magnitude of each gradient indicates how sensitive each factor was to the Spk; the main effects plot is a frequently used method for Taguchi analysis ([16, 34]). When fluence was changed from 0.050 to 0.099 J/cm^2, Spk increased; the increase was more rapid from 0.099 J/cm^2 to 0.149 J/cm^2. A similar behaviour was observed for frequency with the increase from 35 to 52.5 kHz was greater than between 17.5 and 35 kHz. The effect of feed speed showed the opposite behaviour than fluence and frequency. As the feed speed increased from 500 to 1000 mm/s, there was a greater decrease in Spk compared to the very small decrease caused when the feed speed was increased from 1000 to 1500 mm/s. With the hatch distance, there is a decrease in Spk from 0.02 to 0.04 mm but a large increase from 0.04 to 0.06 mm.

Experiment 15 had the highest average Spk value and variation of 4.156 µm and 400%, respectively. This is due to the energy transfer being very high in the areas that are directly exposed to the pulsed laser. These regions resulted in deep grooves on the surface with depth in the region of 10 µm. The larger hatch distance used in this experiment made the surface profile comparable to a textured surface with linear grooves (Figure 7), hence the very high Spk value.

3.1 Surface roughness modelling

Statistical analysis from the Taguchi method and empirical data aided the generation of coefficients used to create the linear model in Equation (2) with a minimised error percentage (1%):

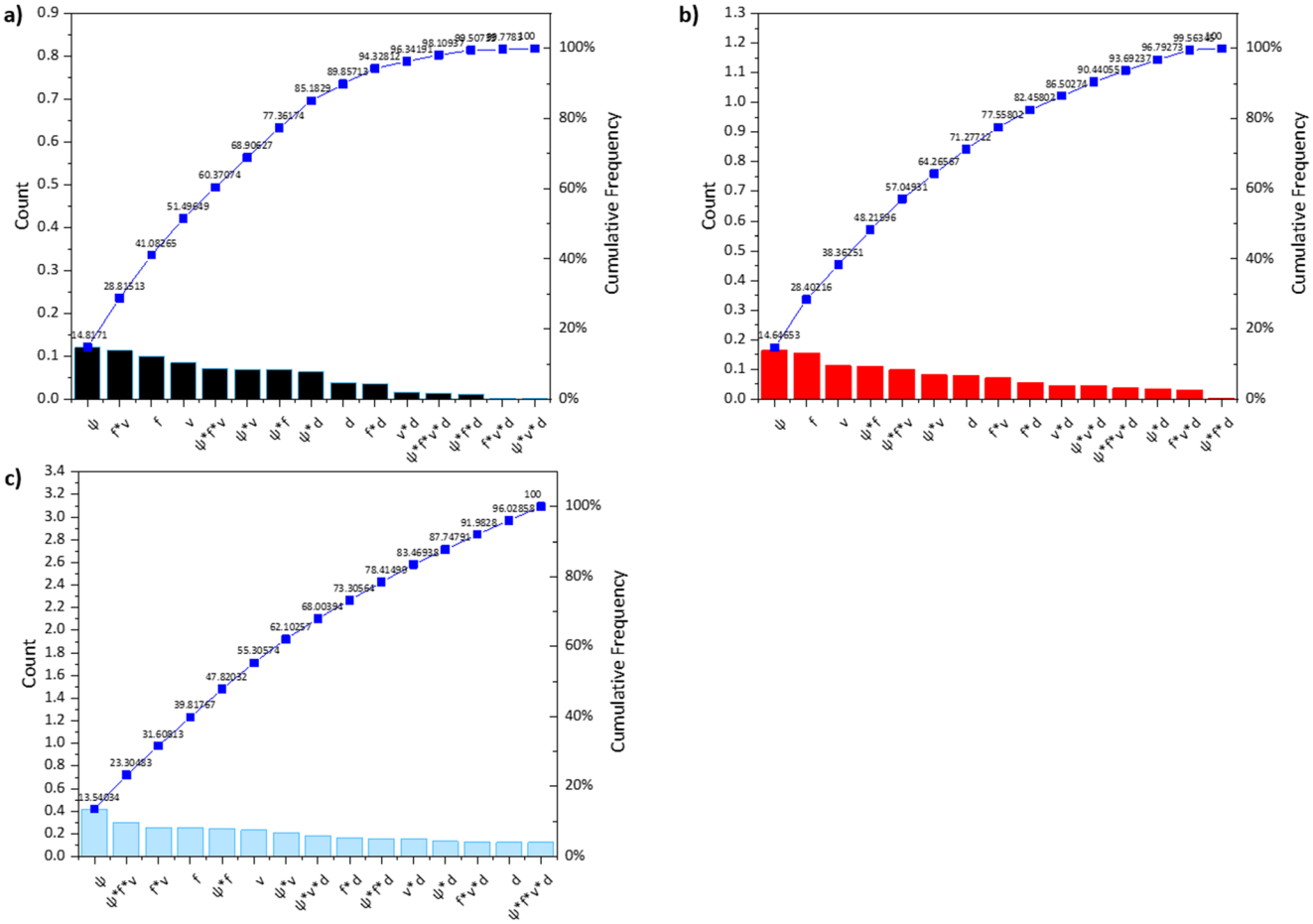

Fig. 5 Pareto effect of each roughness variable based on the parameters chosen. **a** RaV, vertical average roughness, **b** RaH, horizontal average roughness, **c** Spk, reduced peak height

$$Spk_{Model} = 0.9033 + 0.41885\psi + 0.24755\psi f - 0.21025\psi v + 0.13255\psi d - 0.15635vd - 0.30205\psi fv \quad (2)$$

where ψ is fluence (kJ/m^2), f is frequency (MHz), v is speed (m/s) and d is hatch distance (mm).

The parameters included in the equation align with the experimental data investigated in this study. For example, a larger fluence increased the peak distribution as there was more aggressive material melting on the surface leading to more molten material distribution and peaks. The model also takes the interaction effect of parameters to show how they limit or contribute to peaks on the surface. Figure 8 shows this model against the average Spk results measured from experimental data.

The model prioritised fluence and the interaction effects between frequency and speed shown in the previous analysis. It predicted the roughness in the melting region of laser processing with an accuracy of 69%. Eduardo et al. [35] reported a similar accuracy when modelling the melted layer geometry from laser additive manufacturing in Inconel 625 and Iron. The Spk model performed best at moderate to medium level of processing (fluences in the region of 0.050–0.099 J/cm^2) with an error between 1 and 10%. The material removal was approximately less than 0.27 μm^3. When the fluence was 0.149 J/cm^2, there was more violent material melting and expulsion; the material removal was higher than 0.40 μm^3, approximately. The model failed to predict this behaviour accurately with the error percentage between 15 and 36%. This suggests that different models may be needed to fully model the transition from the melting phase to the boiling/vaporisation phase. This is not an uncommon result when studies have attempted to model laser processing. Volpe et al. [36] created a predictive model for the femtosecond laser micro-milling on acrylic (PMMA). The linear model described most of the results but required adaptation using regression was needed to cause certain settings to fall within a good confidence level at higher energy settings. Schatz and Patel [37] also found this with DOE modelling of pulsed laser deposition on lead zirconate titanate (PZT) thin films. Multiple models were generated but no one model perfectly

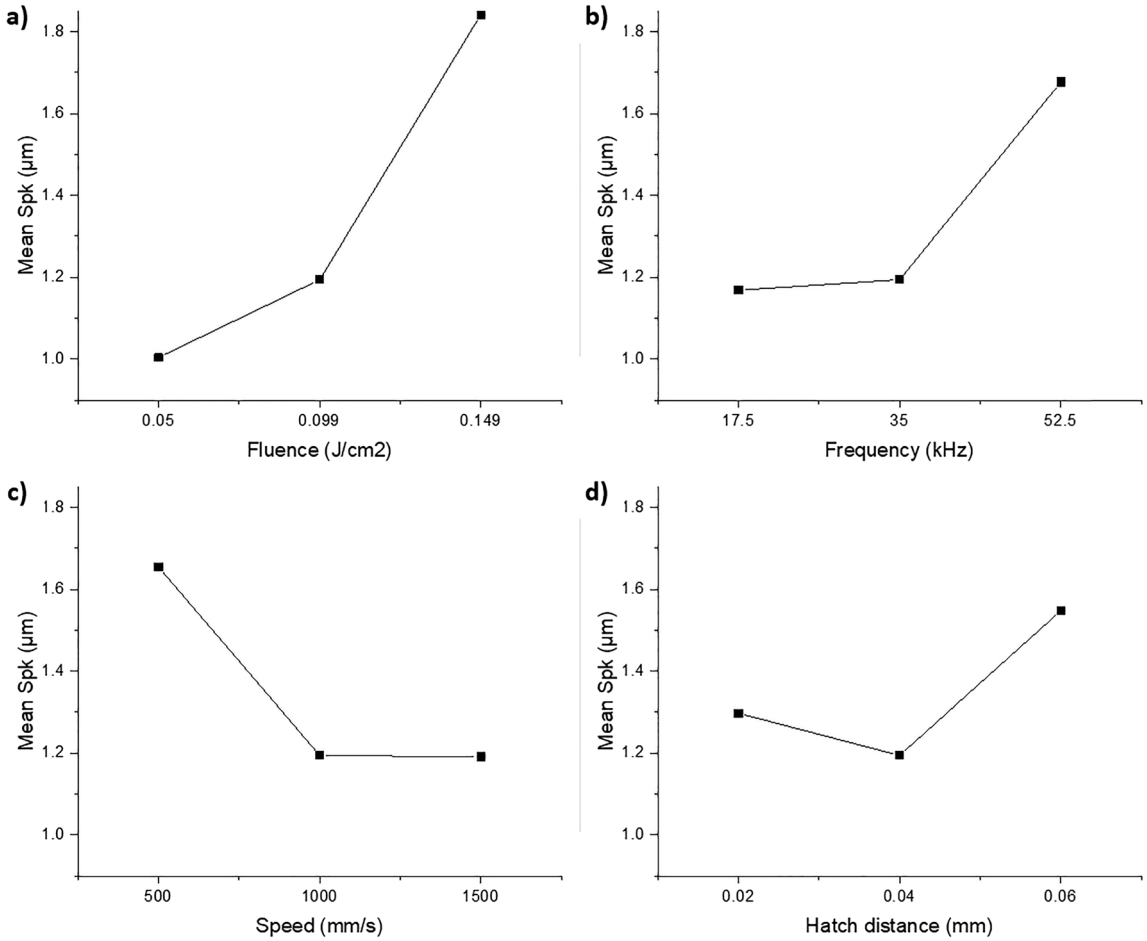

Fig. 6 Main effects of plot: **a** the effect of fluence on Spk, **b** the effect of frequency on Spk, **c** the effect of speed on Spk and **d** the effect of hatch distance on Spk. Larger absolute gradient greater change on surface roughness

fell within a good confidence level, but the study was able to conclude that power and pressure were the most influential factors on the PZT properties.

Fluence caused more melting on the surface and melt redistribution, which increased the chance of microstructural changes and poorer surface. As the cooling rate was not controlled, the solidification rate varied in different regions. Some areas experienced faster cooling leaving small grains and some areas slower cooling leaving larger grains. The mixture of these rate caused voids, porosity and transitional boundaries characterised by peaks on the surface. The trends shown with these parameters are in line with the current material science of laser processing. Davoren et al. [5] studied laser net-shaping WC-Ni9.2% with a fibre laser with powers ranging from 150 to 350 W. A higher power caused a larger molten pool, resulting in a greater change in the microstructure. This created areas of different morphologies of spheroids and fishbone structures, close to the processed area. Xiong et al. [38] presented similar results when laser net-shaping WC-Co, where a higher power created a greater variation in WC particle size causing voids and porosity. There was also a larger HAZ in the surrounding region.

The results of the study and model concluded that fluence is the most influential factor on surface peak generation. The higher energy caused more aggressive material processing and redistribution. This highlighted that fluence is a necessary factor to be optimised to minimise the roughness and have better surface homogeneity overall. The interaction effects of parameters were also significant, indicating that the surface quality cannot solely be optimised using one parameter and parameters cannot be looked at independently. The interaction of fluence and frequency and the interaction of speed and frequency should be considered correlated. A faster speed reduced the number of thermal defects present. However, the frequency had a greater effect on crack formation and the types of cracks formed. The configuration of the linear model generated indicated which parameters contributed most to influencing the surface roughness. Under moderate to medium level of processing, the linear relationship was accurate in describing the resultant surface roughness. It is worth considering the use of quadratic or higher polynomial model for more aggressive processing. The model is significant in providing a better understanding of the laser parameters and the interaction of the laser parameters on the surface integrity of processed WC.

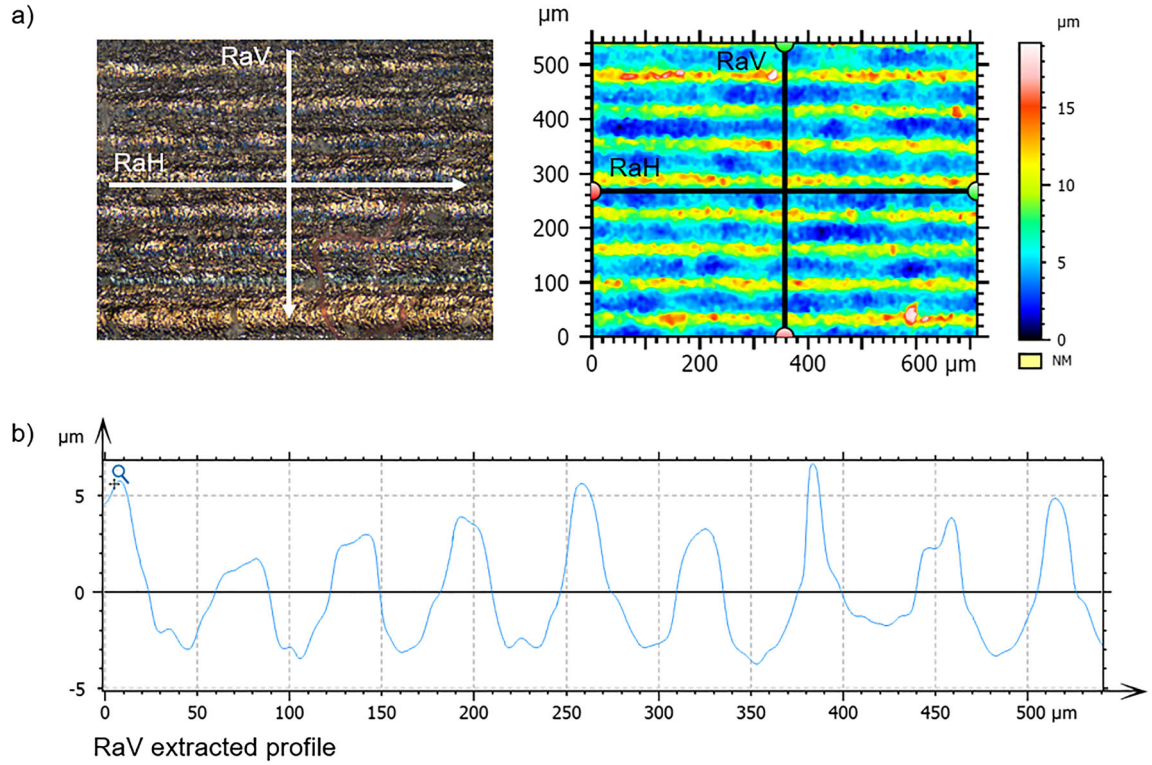

Fig. 7 **a** Roughness profile direction on experiment 15, **b** RaV 2D surface roughness profile for experiment 15 of 2^4 design

3.2 Surface crack optimisation

Cracks are detrimental to the surface integrity and mechanical properties of WC post laser processing ([6, 39]). In this paper, a micro-crack classification system was developed, and a crack density variable was introduced to estimate cracks and crack type on a 1-mm^2 area size. Fluence and frequency settings, between 0.05 and 0.20 J/cm^2 and 5 and 100 kHz, respectively (Table 4), were investigated to isolate these parameters against the crack formation, with a constant feed speed and hatch distance; fluence and frequency settings were investigated. Figure 9 shows the result of the crack density distribution and Figure 10 shows instances of each type of crack at various processing settings. The crack density increased as the fluence increased but peaks at 0.099 J/cm^2 for most frequency settings. Deep cracks were signs of significant damage in the area; on average they did not present until 40 kHz and were situated around balling and splatter defects. Deep cracks were present mostly above 0.099 J/cm^2 across the frequency settings. Micro-cracks were mainly present with the lower fluence settings across the range of frequencies, around the main laser track path area. They were more likely to form between 0.050 and 0.135 J/cm^2. Superficial cracks were present in all frequency settings but particularly with lower fluence settings. This crack type was highest at 0.070 J/cm^2 and 35 kHz. The crack density of each crack type increased between 0.050 and 0.099 J/cm^2 across all frequency settings and then decreased as the fluence increased to 0.20J/cm^2.

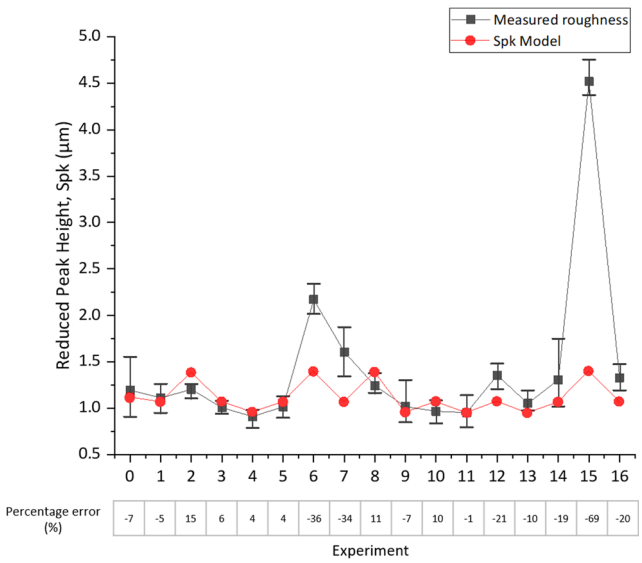

Fig. 8 Model compared against Spk results (with error bars) and percentage error

The transition to thermal shock fracturing can be seen at 0.099 J/cm^2 where there was an equal distribution of the crack types. The lowest density of all three crack types occurred at 0.149 J/cm^2 fluence and 52.5 kHz; the microstructure showed a good amount of melting, uniform material processing and resolidification (Figure 11a). Overall, these results suggested that there was a link between crack defect formation and the variation of fluence and frequency.

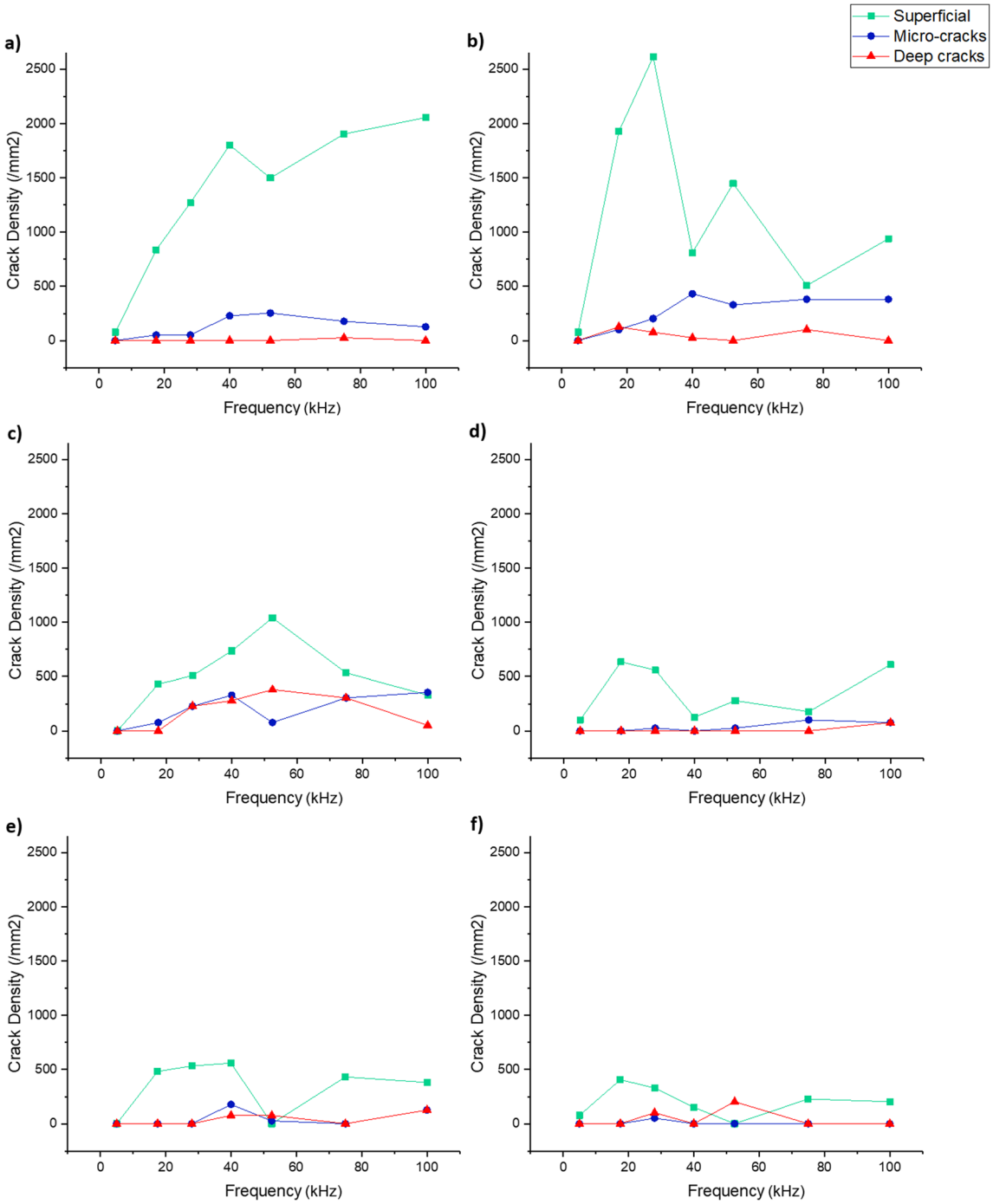

Fig. 9 Crack density against frequency at the following fluence settings: **a** 0.050 J/cm^2 , **b** 0.070 J/cm^2 , **c** 0.099 J/cm^2 , **d** 0.135 J/cm^2 , **e** 0.149 J/cm^2 , **f** 0.200 J/cm^2 (speed 500 mm/s, hatch distance 0.02 mm)

The types of cracks identified on the samples loosely followed a pattern. Superficial cracks were randomly distributed throughout the sample, in no specific regions or areas. Micro-cracks mainly presented within the main laser track area, i.e. along the RaH profile. Deep cracks were found in the overlapping laser track regions. Figure 11b generally shows this crack distribution.

The cracking behaviour of the material was investigated using ANOVA using the crack density variable against fluence and frequency; only these parameters were chosen as they proved to be the first cause of crack formation within the microstructure (see the 'Discussion' section). Table 7 shows the results of this analysis based on fluence and frequency with the percentage influence, calculated

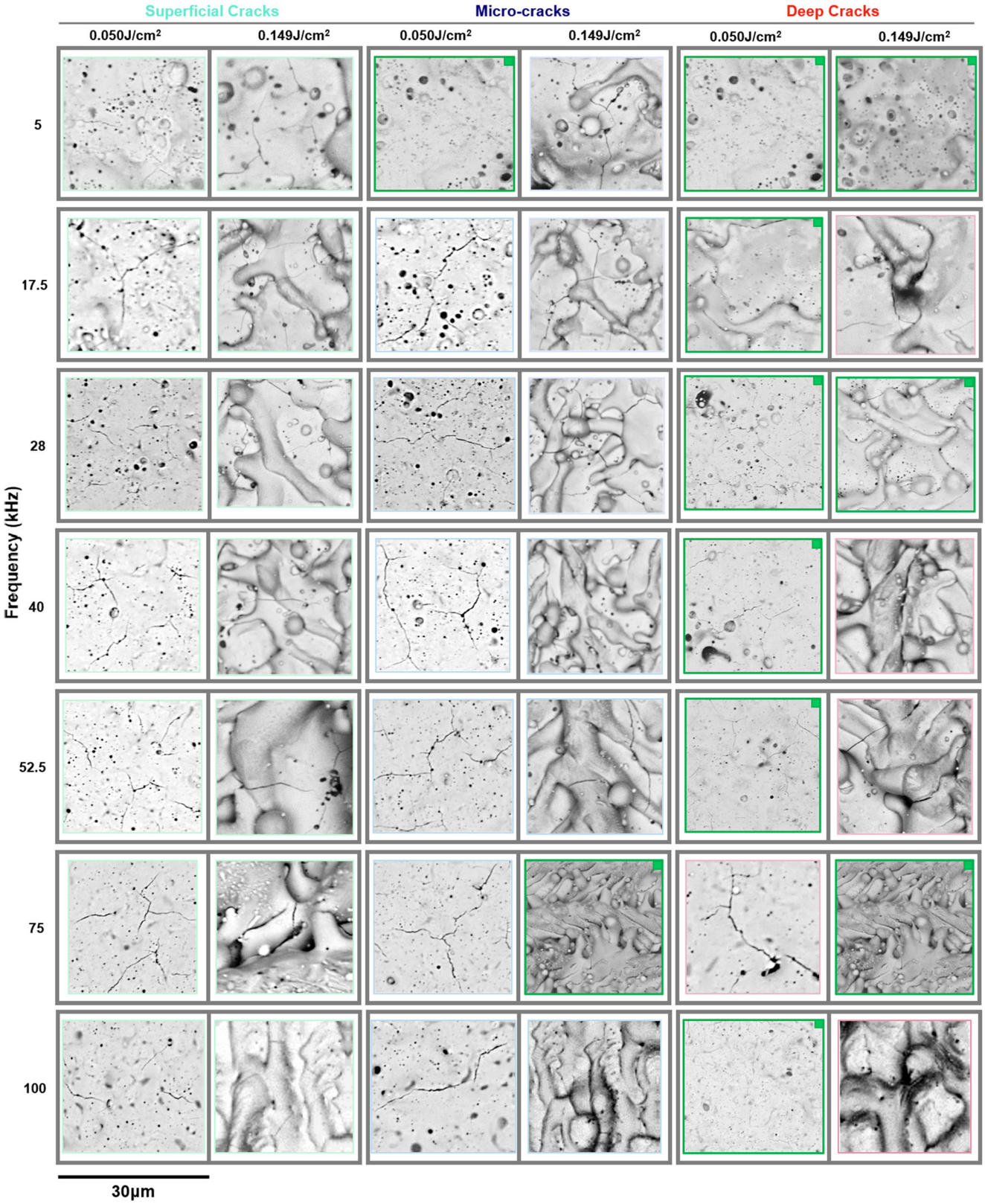

Fig. 10 Crack classification against different fluence and frequency settings, diagrams with a green square mark did not present cracks of that type

using the method described in [40]. The sample size included 147 specimens with a significance level (p value) performed at 10%. The magnitude of the f-statistics paired with a low p value less than 0.1 indicated that fluence and

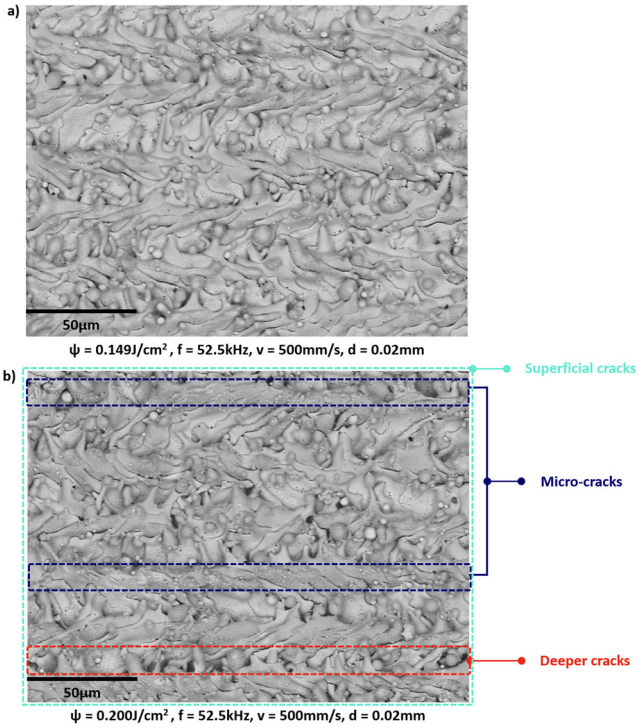

Fig. 11 **a** Minimal cracks with uniform processing, **b** typical location of each type of crack identified

frequency independently had a considerable effect on the crack density. Fluence had a greater contributory magnitude. However, the interaction of fluence and frequency was not a substantial effect in crack density unlike surface roughness. The outcome of this analysis showed that crack generation can be altered by specific laser parameters. Future work should investigate the refinement of the fluence setting to reduce crack formation and subsequently frequency to quantify a threshold based on WC composition and relative laser system setups. The results showed that there was sufficient evidence to support the claim that crack formation can be altered by fluence and frequency independently, but it is not dependent on the interaction of both. This is the first time cracks have been analysed with the statistical process in the laser processing of WC, providing an insight into understanding the key laser parameters on the crack formation mechanism.

4 Discussion

The as-received microstructure had a highly homogeneous crystallinity (Figure 12). Experiments referenced in this section refer to Table 3. The processed samples showed different levels of discoloration; samples processed at 0.149 J/cm^2 and 52.5 kHz had noticeable regions of darker regions indicative of burning. In these regions, there was a high percentage of carbon (Table 8), possibly due to the high energy causing material disassociation on the sample (Figure 13). This is an effect when WC is exposed to high temperatures, causing the carbon in the WC phases to diffuse into the binder phases [41]. For example, Chen et al. [42] found this in the laser additive manufacturing of WC-reinforced iron and Bartkowski et al. [43] noticed this effect when laser cladding Fe/WC on low carbon steel.

Majority of the samples had a distinct HAZ around the 1-mm^2 processing region, with a border of approximately 0.25 mm; this is expected as carbides often suffer from HAZ to different degrees depending on the processing parameters. Dumitru et al. [15] explained this is due to the small optical penetration depth of WC, which causes heat diffusion in the laser processing area. The microstructure of the laser-treated surfaces indicated that temperature was too low for the surface to properly melt all phases of the material [44, 45]. The binder and WC phase were thermally excited to different extents due to the difference in thermal properties within the material (Table 9 [46]). This resulted in the array of cracks throughout the surface by the expansion and contraction of the binder.

4.1 Effect of fluence and speed on material processing

Fluences above 0.099 J/cm^2 resulted in a significantly changed microstructure where there was a lot of molten material redistribution. This is caused by the photon momentum of the process [47]—causing a splatter/splotchy geometry; these features had a diameter of around 45 µm (Figure 14a).

The ridges surrounding the circular geometries explained the increase of peaks and valleys on the surface. Analytically fluence had the greatest effect on peaks on the surface; this is also the case on a microstructural level. When comparing all the samples that were processed at 0.149 J/cm^2, they had a

Table 7 ANOVA results for crack density using fluence and frequency

Source	Type III sum of squares	df	Mean square	f-statistic	*p* value	Percentage influence (%)
Fluence	8492.892	2	4246.446	**6.493**	**0.004**	63.49
Frequency	3930.630	2	1965.315	**3.005**	**0.061**	29.38
Frequency * Fluence	1906.973	4	476.743	**0.729**	**0.578**	7.13

a. *R*-squared = 0.352 (adjusted *R*-squared = 0.222)

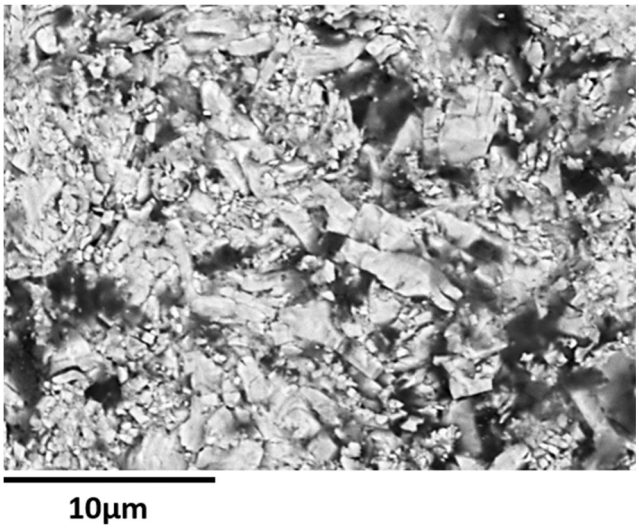

Fig. 12 Microstructure of the as-received WC sample

Table 8 Chemical composition at burnt regions within samples

Element	C	O	Co	W	Al	Si
wt%	50.5	16.7	7.5	22.3	0.3	2.0

resembling microstructure despite changing the other parameters. This indicated that there was a fluence threshold, between 0.099 J/cm^2 and 0.149 J/cm^2 on the WC structure, above which fluence dictated the resulting microstructure. All the experiments processed at 0.050 J/cm^2 had greater variation in appearance and surface morphology suggesting other parameters take precedent on the resultant microstructure.

Experiments processed with 0.149 J/cm^2, 52.5 kHz and 500 mm/s transferred the most amount of laser energy; they appeared burnt and had the most remelting in the region (Figure 14b, Figure 14d). This is as expected as the high fluence and frequency paired with the slower speed prolonged the amount of energy delivered—giving time for the

Table 9 Thermal properties of materials associated with Tungsten Carbide [46].

	WC	Co
Thermal conductivity (α_1), Wm^{-1}K^{-1}	110	100
Thermal expansion coefficient (κ), µK^{-1}	5.5	13

workpiece to heat and melt but not ablate ([15, 48]). In some samples, the laser raster pattern was evidenced by material peaks and bulges of remelted material (Figure 14e). The effect of fluence on the surface topography is shown in Figure 15. The 0.149 J/cm^2 fluence caused more melting, with material migration resolidified on the surface giving the splatter like appearance referred to before. There were also fewer cracks, transverse to the laser beam path. Marimuthu et al. [1] found a similar trend when using picosecond laser to process WC. As the fluence increased the material removal and crater roughness increased, however less cracking damage was present in the surrounding microstructure. The 0.050 J/cm^2 samples exhibited smaller circular regions of melt expulsion and voids with a greater distribution of cracks.

Increasing the speed showed a clear improvement in the quality of surfaces. Speed dictated how long each area of the workpiece was exposed to the laser and changed the amount of energy deposited. A slower speed increased the amount of thermal damage to the surface giving rise to a range of defects. The samples processed with the faster speed of 1500 mm/s had a more homogeneous surface in relation to uniformity and the distribution of defects. This was attributed to the laser energy causing localised heating and the momentum of the process distributing molten material causing splatter to spread through multiple laser tracks (Figure 16b). A slower speed concentrated more heat in specific areas, giving rise to even more splatter and localised defects (Figure 16a).

Speed also altered the general response of the material to the laser. Experiment 3 showed significant thermal shock evidenced by numerous superficial and micro-cracks

Fig. 13 Burnt regions in samples

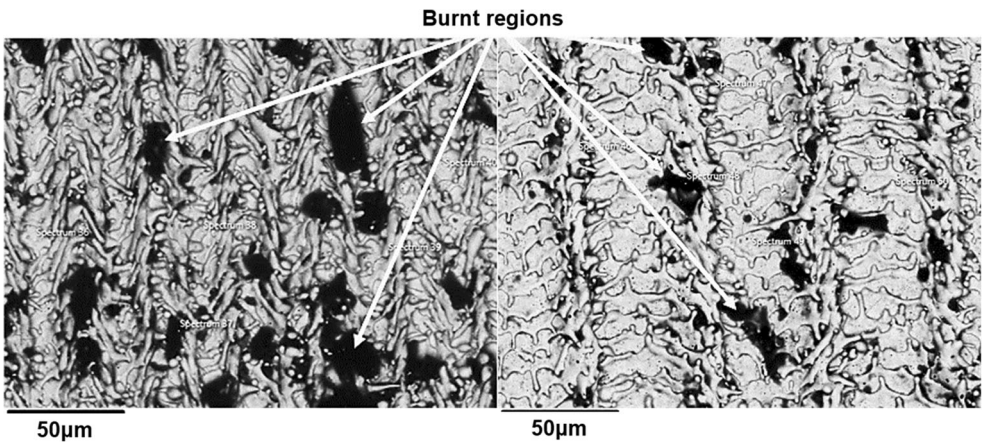

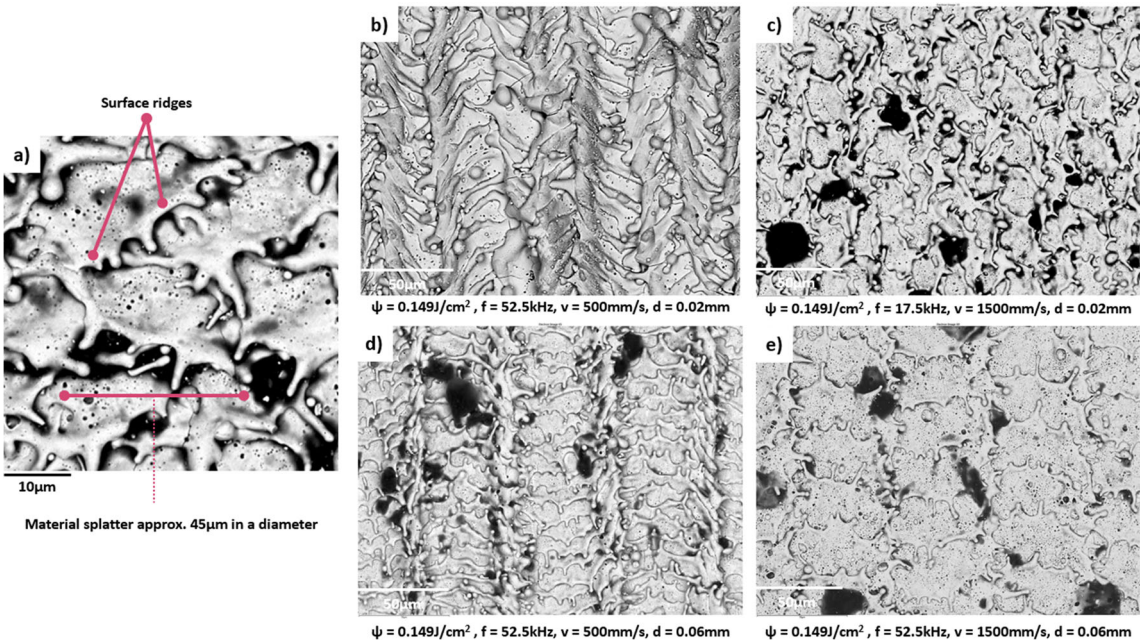

Fig. 14 **a** Surface remelting and splatter geometry from laser processing, **b** experiment 6, **c** experiment 7, **d** experiment 15, **e** experiment 16

(Figure 17). This was a result of the slow speed and higher frequency combination, as other samples processed with 500 mm/s and 52.5 kHz also presented a similar crack distribution. The WC grades used in this study had a relatively low WC content with a greater presence of the cobalt binder. As the WC and binder have very different thermal expansion coefficients, 5.5 μK^{-1} and 13 μK^{-1}, respectively; each constituent expands at a different rate causing internal stresses and cracks. This was also demonstrated in the SLS of WC-Co by Paul et al. [6], where the rapid cooling of the cobalt phase caused high surface tensions in the molten pool. This caused cracks and geometric distortions. A higher weight percentage of WC would reduce this effect if the same parameters were used as less of the binder would be present to induce stresses [30]. Khmyrov et al. [39] showed this when laser sintering WC-Co of equal weight percentages and found many cracks due to the formation of W_3Co_3C brittle phases.

A further look into speed on the material processing was done using the 0.050 J/cm^2 to limit the effect of fluence on the surface (Figure 18).

At slower speed, there is a greater build-up of heat allowed for greater energy transfer. This increased the likelihood of the thermal mismatch, which presented as cracks and voids particularly at the carbide/binder interface [12]. At 250 mm/s, cracks were concentrated and prevalent near voids (Figure 19). As the speed increased, there was more irregular heating causing porosity (Figure 19). At 750 mm/s, the voids became larger and more frequent on the surface (Figure 20). The fastest speed of 2500 mm/s exhibited regions of barely processed areas surrounded by porosity (Figure 21); from the

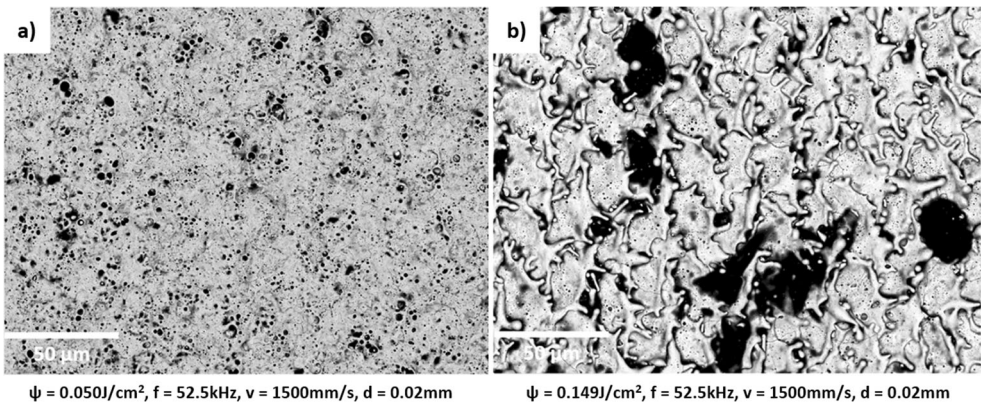

Fig. 15 **a** Experiment 9 and **b** experiment 12

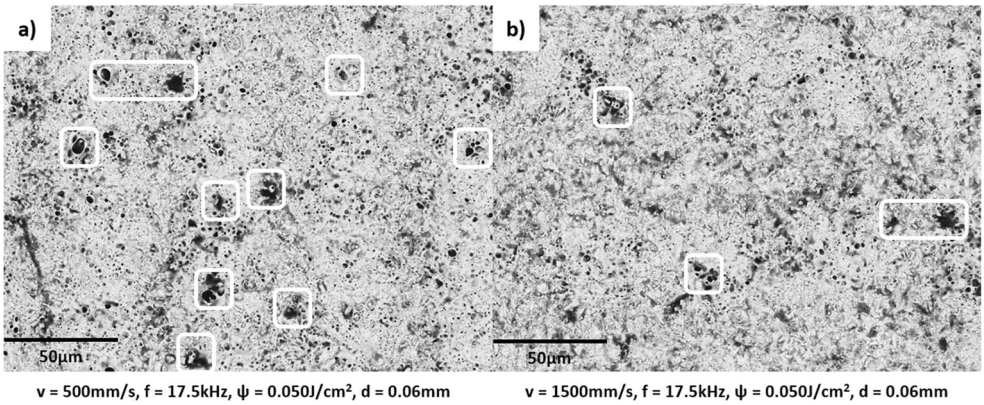

Fig. 16 **a** Experiment 5, **b** experiment 11. White squares represent localised defects

non-uniform heating and rapid solidification, restricting the material's ability to melt and remelt uniformly [49].

4.2 Effect of frequency on the fracture mechanism

Frequency affected the amount of energy the laser transferred to the surface; the higher the frequency the greater the potential heating effect. Previous analysis showed that frequency was a clear factor in crack formation on the surface [6]. As frequency had such a dramatic effect on the surface, a further inquiry into material response was conducted. Figure 22 shows the result using higher frequency levels. SEM analysis showed that thermal excitation at the high frequency changed the material response to crack generation.

At the lowest frequency of 5 kHz, there was a heterogeneous energy distribution demonstrated by the clear regions of material transition, similar to when a large hatch distance is used (Figure 22a). The boundary laser regions and overlapping tracks was characterised by voids, balling, and irregular pores (Figure 23). At 17.5 kHz, the surface showed more mechanical effects of cracking; with time for molten material to distribute (Figure 22b). The thermal response from the laser, from 40 kHz, began to dominate the morphological changes, altering the characteristics of the cracks and defects balling became more pronounced and frequent (Figure 24); caused by Marangoni convections from the higher temperature gradient. This caused the material to solidify before spreading along the surface. This phenomenon has mainly been found in SLS. Zhou et al. [50] studied the balling of pure tungsten with SLS by changing the laser exposure time. A longer laser exposure time caused thermal convection currents in the molten pool making the balling more distinct and larger. This balling defect has also been present in other materials. Khairallah et al. [51] investigated the physics of laser powder bed fusion of stainless steel and found that the balling effect is a result of the surface tensions. The balling was minimised by controlling the heat concentration on the laser processed area. From 52.5 kHz, a greater heat accumulation in the surface caused more remelting and splatter like regions. The movement of splatter was also confined to the width of the laser track indicating insufficient time to distribute around the surface (Figure 22e). The 100-kHz frequency setting had a distinct surface morphology, with fewer defects of balling and spherical pores (Figure 25). It was evident from this that there was a progressive transition from mechanically induced stress from the laser to a thermally driven response. This trend has

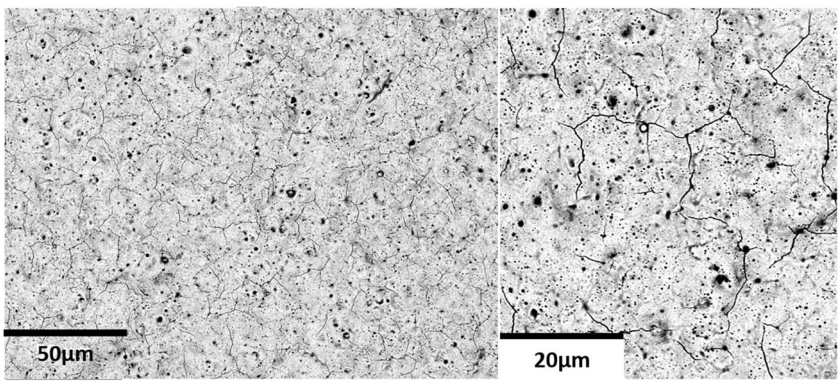

Fig. 17 Thermal shock demonstrated in experiment 3

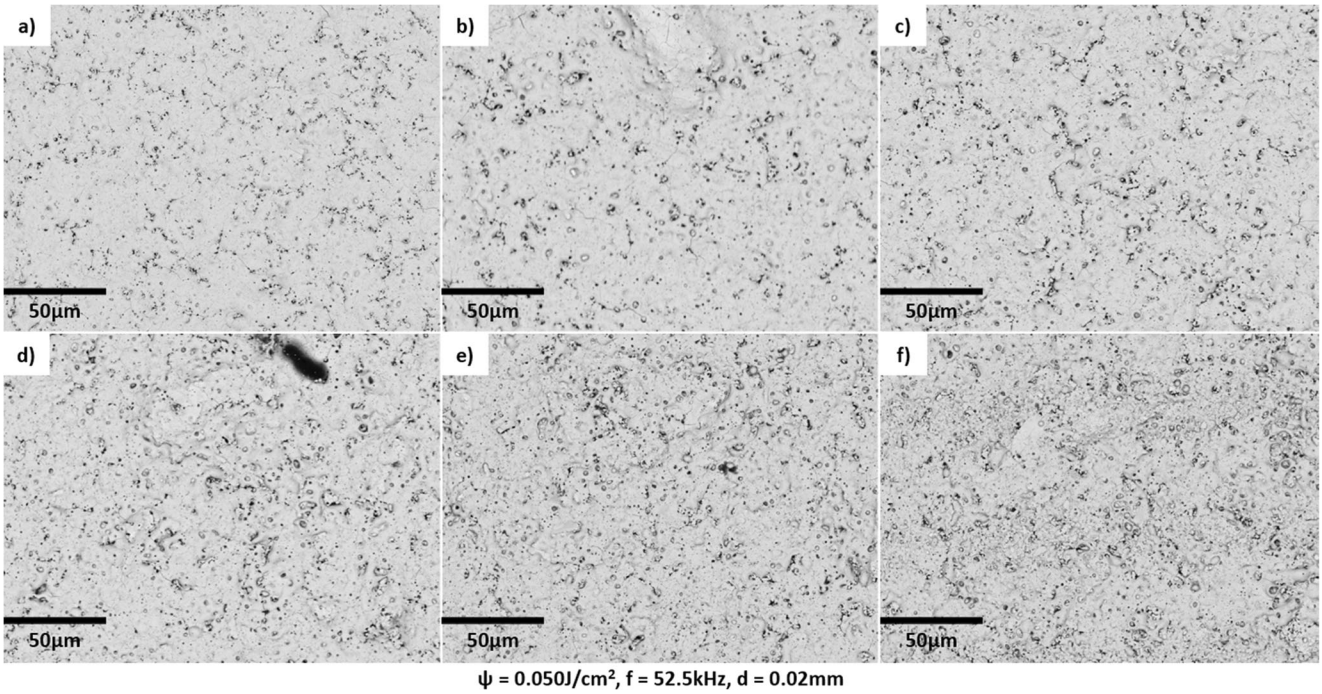

Fig. 18 Microstructure of workpiece when processed at different speeds: **a** 250 mm/s, **b** 500 mm/s, **c** 750 mm/s, **d** 1000 mm/s, **e** 1500 mm/s, **f** 2500 mm/s

also been seen in the laser processing of gold alloy thin films by Geremia et al. [52].

5 Conclusion

The presented findings show insights in understanding the surface integrity of laser surface engineered tungsten carbide. The material response to different laser process parameters (fluence, frequency, speed and hatch distance) was evaluated, using a pulsed fibre laser at 1060-nm wavelength in the ns regime pulse duration. The conclusions are summarised:

- The study shows a need to understand the relationship between the laser parameters chosen for processing WC. Laser-induced damage on WC ranged from cracking, thermal shock, porosity, balling, HAZ, splatter and spherical pores. The parameters altered the amount of energy delivered to the workpiece material. Fluence was the most influential factor on the surface roughness and microstructure. It dictated the morphology of features (> 0.149 J/cm^2) in the processed regions in a splatter-like geometry, which in turn increased the surface roughness. Increasing the frequency (5–100 kHz) caused a progressive transition from mechanically induced stress to a thermally driven response, with more thermal defects notably balling. Feed speed had the greatest effect on defects such as voids and porosity. Slower speeds (250–750 mm/s) caused concentrated heated areas, giving rise to localised defects, e.g. pores, porosity, and increased the likelihood of thermal shock. At higher speeds (> 2000 mm/s), the microstructure exhibited regions of barely processed areas

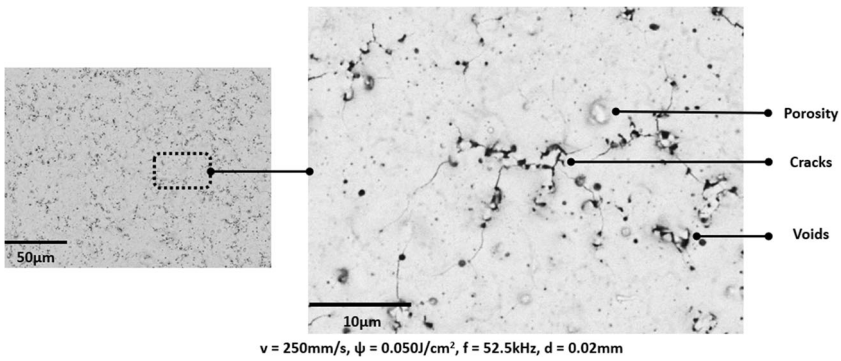

Fig. 19 250 mm/s feed speed result

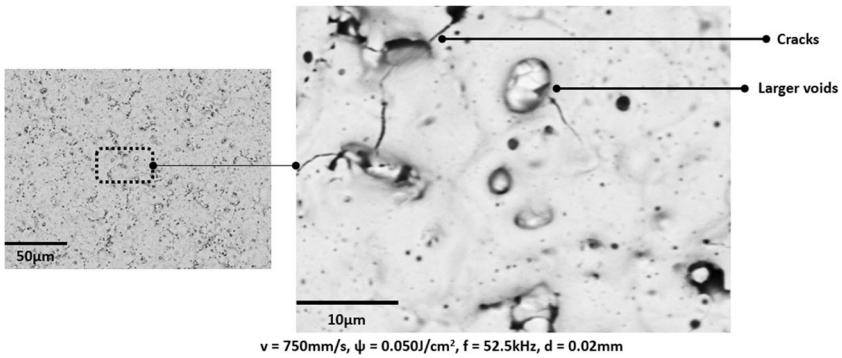

Fig. 20 750 mm/s feed speed result

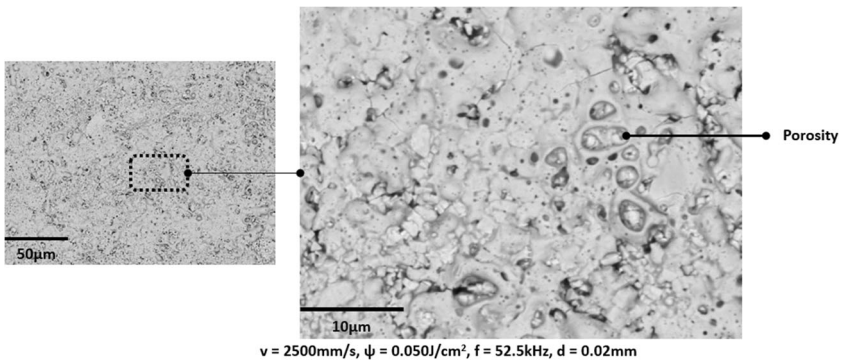

Fig. 21 2500 mm/s feed speed result

surrounded by porosity from non-uniform heating and rapid solidification, restricting the material's ability to melt and remelt uniformly.

- The crack classification system was useful for objective and quantitative analysis. It classified cracks into 3 groups: superficial, micro-cracks and deep cracks based on size and damage. A crack density variable was calculated to estimate the number of cracks and crack type within a 1-mm^2 area size based on the laser parameters. Despite this, the process is still a rough approximation and

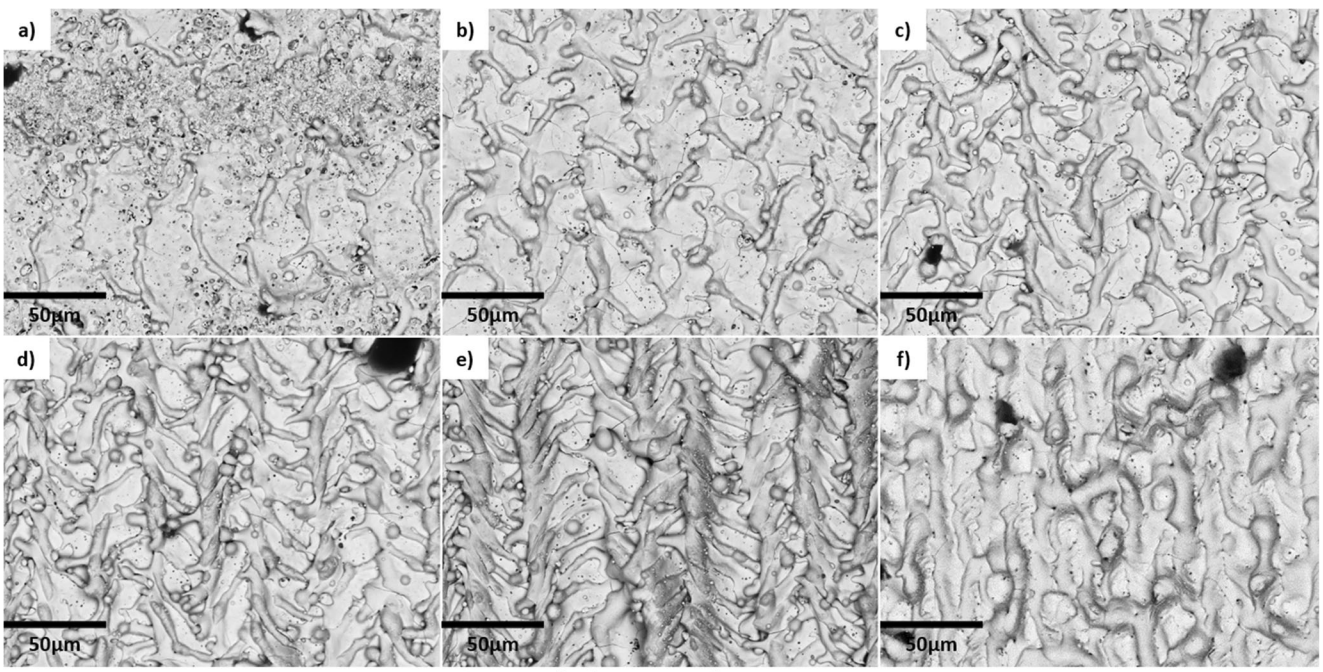

Fig. 22 Microstructure of workpiece when processed at different frequencies: **a** 5 kHz, **b** 17.5 kHz, **c** 28 kHz, **d** 40 kHz, **e** 52.5 kHz and **f** 100 kHz

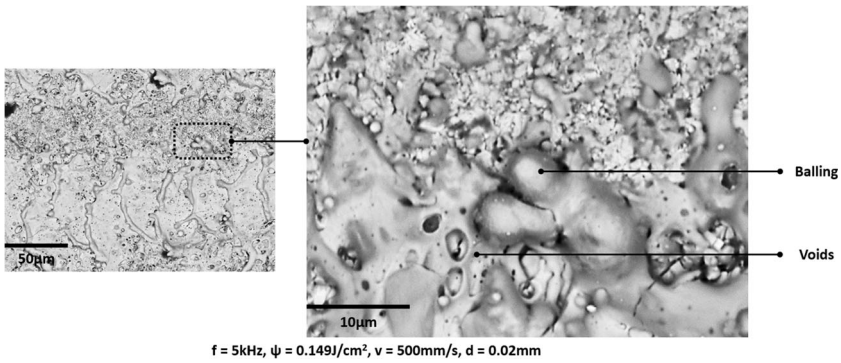

Fig. 23 5-kHz frequency result

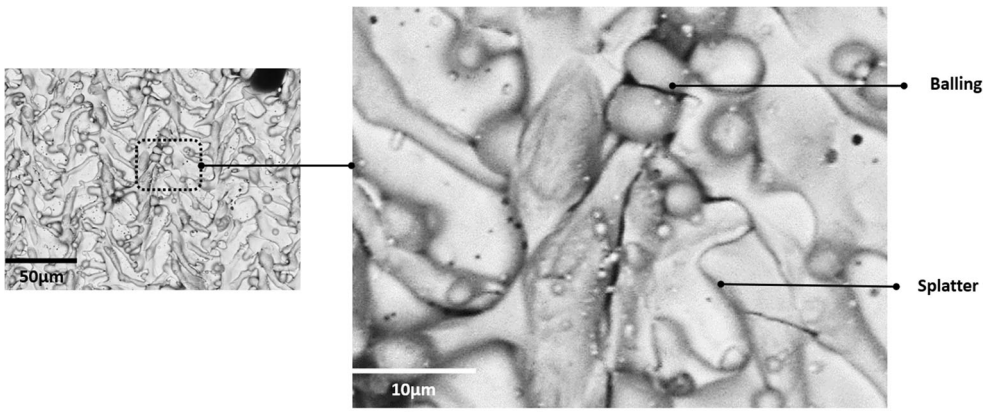

Fig. 24 40-kHz frequency result

is not automated, future research will investigate the use of computer processing techniques, e.g. pixel analysis, to improve the robustness of crack identification and classification.

- For minimising the crack density, fluence (63.49 %) and frequency (29.38 %) had a significant effect on the crack density independently but not the interaction of both (7.13 %). The crack density increased between 0.050 and 0.099 J/cm^2 across all frequency settings then decreased as the fluence increased to 0.20 J/cm^2. Superficial cracks were present in all frequency settings but particularly with lower fluence settings. Micro-cracks were more likely to form between 0.050 and 0.135 J/cm^2. Deep cracks did not present until 40 kHz or above 0.099 J/cm^2 across the frequency settings and were situated around balling and splatter defects.
- A linear model to predict surface roughness was proposed based on the experimental Taguchi analysis. It performed best when there was a moderate to medium level of processing (0.050–0.099 J/cm^2), with an error between 1 and 10 % but failed to accurately model the behaviour when there was more violent material melting (> 0.099 J/cm^2),

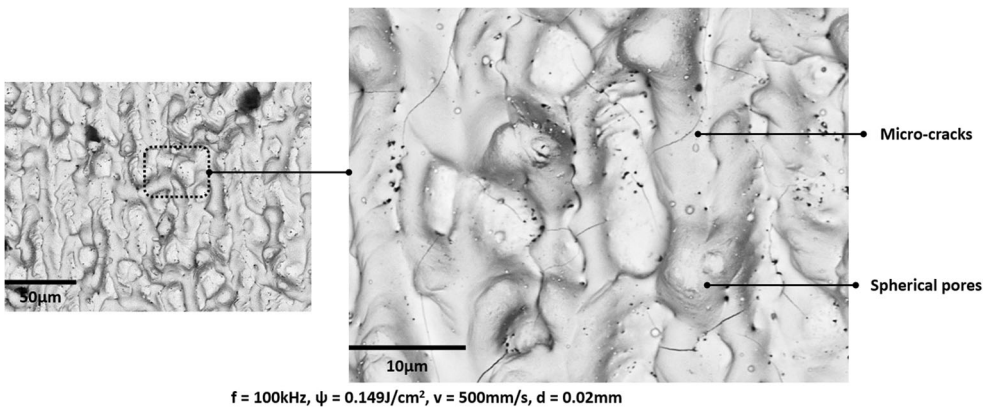

Fig. 25 100-kHz frequency result

with an error between 15 and 36 %. It can be concluded that the interaction of parameters is as important to optimise as the parameters themselves independently. This process showed the laser process can be modelled however different models may be required to describe the behaviour at different processing states, i.e. melting or ablation.

- To build more confidence in the robustness of optimisation, more advanced modelling techniques will be considered including artificial intelligence (AI) and deep learning. These methods can handle a greater number of parameters and settings to analyse the surface integrity. AI processing can also aid in inspecting surface cracks with visual inspection techniques. The aim of study was to develop a method to understand and control the laser processing of brittle materials to retain the surface integrity for various applications.
- The findings of the present work are important as they provide a basic framework for understanding the material science interaction during the laser processing of WC and how dependent the factors are on the microstructure of samples. In particular, cracks induced within the microstructure have an impact on tool performance in industrial applications, limiting the life. On the other hand, specific features, e.g. textures, generated on the microstructure may be advantageous to certain machining applications. The optimisation of laser parameters can minimise defects and control the generation of specific features.

Supplementary Information The online version contains supplementary material available at https://doi.org/10.1007/s00170-021-07885-8.

Acknowledgements The authors would like to acknowledge the assistance of Shaun Fowler in the Loughborough Materials Characterisation Centre (LMCC).

Author contribution All authors contributed to the work with the order provided.

Funding The research leading to these results received funding from the Manufacturing Technology Centre (MTC) in support of the Ph.D studentship.

Data Availability Not applicable.

Declarations

Ethical approval Not applicable.

Consent to participate Not applicable.

Consent to publish All authors have reached agreement for publication.

Competing interests The authors declare that they have no conflict of interest.

References

1. Marimuthu S, Dunleavey J, Smith B (2020) Picosecond laser machining of tungsten carbide. Int J Refract Met Hard Mater 92(105): 3–38. https://doi.org/10.1016/j.ijrmhm.2020.105338
2. Smith GT (2008) Cutting Tool Technology. London, UK
3. Pacella M (2019) A new low-feed chip breaking tool and its effect on chip morphology. Int J Adv Manuf Technol 104(1-4):1145–1157. https://doi.org/10.1007/s00170-019-03961-2
4. Schwarzkopf P, Kieffer R, Leszynski W, Benesovky F (1960) Cemented carbides. London
5. Davoren B, Sacks N, Theron M (2019) Laser engineered net shaping of WC-9.2wt%Ni alloys: A feasibility study. Int. J. Refract. Met. Hard Mater 86(2019):105–136. https://doi.org/10.1016/j.ijrmhm.2019.105136
6. Paul S, Singh R, Yan W (2016) Lasers based manufacturing. New Dehli, India
7. Lee C, Park H, Yoo J, Lee C, Woo W, Park S (2015) Residual stress and crack initiation in laser clad composite layer with Co-based alloy and WC + NiCr. Appl Surf Sci 345:286–294. https://doi.org/10.1016/j.apsusc.2015.03.168
8. Hasselman DPH (1969) Unified theory of thermal shock fracture initiation and crack propagation in brittle ceramics. J Am Ceram Soc 52(11):600–604. https://doi.org/10.1111/j.1151-2916.1969.tb15848.x
9. Wu Z (2015) The mechanism governing cutting of hard materials with hybrid laser / waterjet system through controlled fracture. Dissertation, Iowa State University
10. Herd S, Wood RJK, Wharton JA, Higgs CF (2018) Explicit fracture modelling of cemented tungsten carbide (WC-Co) at the mesoscale. Mater Sci Eng A 712(2018):521–530. https://doi.org/10.1016/j.msea.2017.11.109
11. Wang B, Wang Z, Yuan J, Yin Z, Huang L, Zheng K (2020) High temperature fracture mechanism of ultrafine WC-Co cemented carbides containing (Ti,W)C. Int J Refract Met Hard Mater 95(2020): 105428. https://doi.org/10.1016/j.ijrmhm.2020.105428
12. Sigl LS, Exner HE (1987) Experiemental study of the mechanics of fracture in WC-Co alloys. Metall Trans A, Phys Metall Mater Sci 18(7):1299–1308. https://doi.org/10.1007/BF02647199
13. Novikov NV, Dub SN (1996) Hardness and fracture toughness of CVD diamond film. Diam Relat Mater 5(9):1026–1030. https://doi.org/10.1016/0925-9635(95)00346-0
14. Mao C, Sun X, Huang H, Kang C, Zhang M, Wu Y (2016) Characteristics and removal mechanism in laser cutting of cBN-WC-10Co composites. J Mater Process Technol 230(2016):42–49. https://doi.org/10.1016/j.jmatprotec.2015.11.014
15. Dumitru G, Romano V, Weber HP, Sentis M, Marine W (2002) Femtosecond ablation of ultrahard materials. Appl Phys A Mater Sci Process 74(6):729–739. https://doi.org/10.1007/s003390101183

16. Öztürk B, Kara F (2020) Calculation and estimation of surface roughness and energy consumption in milling of 6061 alloy. Adv Mater Sci Eng 2020:1–12. https://doi.org/10.1155/2020/5687951
17. Ayyildiz EA, Ayyildiz M, Kara F (2021) Optimization of surface roughness in drilling medium-density fiberboard with a parallel robot. Adv Mater Sci Eng 2021:1–8. https://doi.org/10.1155/2021/6658968
18. Kara F, Köklü U, Kabasakaloğlu U (2020) Taguchi optimization of surface roughness in grinding of cryogenically treated AISI 5140 steel. Mater Test 62(10):1041–1047. https://doi.org/10.3139/120.111583
19. Pacella M, Nekouie V, Badiee A (2019) Surface engineering of ultra-hard polycrystalline structures using a nanosecond Yb fibre laser. J Mater Process Technol 266(2019):311–328. https://doi.org/10.1016/j.jmatprotec.2018.11.014
20. Karpuschewski B, Schmidt K, Prilukova J, Beňo J, Maňková I, Hieu NT (2013) Influence of tool edge preparation on performance of ceramic tool inserts when hard turning. J Mater Process Technol 213(11):1978–1988. https://doi.org/10.1016/j.jmatprotec.2013.05.016
21. Kacar E, Mutlu M, Akman E, Demir A, Candan L, Canel T, Gunay V, Sinmazcelik T (2009) Characterization of the drilling alumina ceramic using Nd:YAG pulsed laser. J Mater Process Technol 209(4):2008–2014. https://doi.org/10.1016/j.jmatprotec.2008.04.049
22. Wang Y, Molian P, Shrotriya P (2014) Crack separation mechanism in CO2 laser machining of thick polycrystalline cubic boron nitride tool blanks. Int J Adv Manuf Technol 70(5-8):1009–1022. https://doi.org/10.1007/s00170-013-5312-3
23. Calderón Urbina JP, Daniel C, Emmelmann C (2013) Experimental and analytical investigation of cemented tungsten carbide ultrashort pulse laser ablation. Phys Procedia 41:752–758. https://doi.org/10.1016/j.phpro.2013.03.144
24. See TL, Liu Z, Liu H, Li L, Chppendale J, Cheetham S, Dilworth S (2015) Effect of geometry measurements on characteristics of femtosecond laser ablation of HR4 nickel alloy. Opt Lasers Eng 64:71–78. https://doi.org/10.1016/j.optlaseng.2014.07.011
25. Pacella M, Axinte DA, Butler-Smith PW, Daine M (2014) On the topographical/chemical analysis of polycrystalline diamond pulsed laser ablated surfaces. Procedia CIRP 13:387–392. https://doi.org/10.1016/j.procir.2014.04.066
26. Dahotre NB, Harimkar S (2008) Laser fabrication and machining of materials. New York, USA
27. Metzner D, Lickschat P, Weißmantel S (2019) Laser micromachining of silicon and cemented tungsten carbide using picosecond laser pulses in burst mode: ablation mechanisms and heat accumulation. Appl Phys A Mater Sci Process 125(7):1–8. https://doi.org/10.1007/s00339-019-2755-x
28. Wang X, Wan W, Zheng H (2019) Picosecod laser micromachining of tungsten carbide. Industrial Laser Solution. https://www.industrial-lasers.com/micromachining/article/14039508/picosecond-laser-micromachining-of-tungsten-carbide
29. Eberle G, Wegener K (2014) Ablation study of WC and PCD composites using 10 picosecond and 1 nanosecond pulse durations at green and infrared wavelengths. Phys Procedia 56(C):951–962. https://doi.org/10.1016/j.phpro.2014.08.115
30. Klünsner T, Lube T, Gettinger C, Walch L Pippan R (2020) Influence of WC-Co hard metal microstructure on defect density, initiation and propagation kinetics of fatigue cracks starting at intrinsic and artificial defects under a negative stress ratio. Acta Mater 188(2020):30–39. https://doi.org/10.1016/j.actamat.2020.01.057
31. Denkena B, Grove T Theuer M (2018) Micro crack formation in hardmetal milling tools. Int J Refract Met Hard Mater 70(2018):210–214. https://doi.org/10.1016/j.ijrmhm.2017.10.008
32. Mishra S, Yadava V (2015) Laser beam micromachining (LBMM) - a review. Opt Lasers Eng 73(2015):89–122. https://doi.org/10.1016/j.optlaseng.2015.03.017
33. Stephanie F, Mike O, Ben T, John Z (2006) Design of experiments via taguchi methods: orthogonal arrays. LibreTexts 1-11. https://controls.engin.umich.edu/wiki/index.php/Design_of_experiments_via_taguchi_methods:_orthogonal_arrays
34. Canel T, Zeren M, Sınmazçelik T (2019) Laser parameters optimization of surface treating of Al 6082-T6 with Taguchi method. Opt Laser Technol 120(2020):105714. https://doi.org/10.1016/j.optlastec.2019.105714
35. Eduardo L, Santos H, Pereira M, Lindolfo W, Oliveira L (2021) Modeling layer geometry in directed energy deposition with laser for additive manufacturing. Surf Coat Technol 409(2020):216897. https://doi.org/10.1016/j.surfcoat.2021.126897
36. Volpe A, Trotta G, Krishnan U, Ancona A (2019) Prediction model of the depth of the femtosecond laser micro-milling of PMMA. Opt Laser Technol 120(2019):105713. https://doi.org/10.1016/j.optlastec.2019.105713
37. Schatz A, Pantel D, Hanemann T (2016) Application of DoE methods to establish a model for the pulsed laser deposition of PZT thin-films. IEEE Int. Symp. Appl. Ferroelectr. Eur. Conf. Appl. Polar Dielectr. Piezoelectric Force Microsc. ISAF(2016):2-5
38. Xiong Y, Smugeresky JE, Schoenung JM (2009) The influence of working distance on laser deposited WC-Co. J Mater Process Technol 209(10):4935–4941. https://doi.org/10.1016/j.jmatprotec.2009.01.016
39. Khmyrov RS, Safronov VA, Gusarov AV (2016) Obtaining crack-free WC-Co alloys by selective laser melting. Phys Procedia 83(2016):874–881. https://doi.org/10.1016/j.phpro.2016.08.091
40. Camposeco-Negrete C (2013) Optimization of cutting parameters for minimizing energy consumption in turning of AISI 6061 T6 using Taguchi methodology and ANOVA. J Clean Prod 53(2013):195–203. https://doi.org/10.1016/j.jclepro.2013.03.049
41. ElementSix (2016) The Element Six CVD Diamond Handbook. Berkshire, UK
42. Chen H, Gu D, Kosiba K, Lu T, Deng L, Xi L Kühn U (2020) Achieving high strength and high ductility in WC-reinforced iron-based composites by laser additive manufacturing. Addit Manuf 35(2020):101195. https://doi.org/10.1016/j.addma.2020.101195
43. Bartkowski D, Bartkowska A, Jurči P (2021) Laser cladding process of Fe/WC metal matrix composite coatings on low carbon steel using Yb: YAG disk laser. Opt Laser Technol 136(2020):106784. https://doi.org/10.1016/j.optlastec.2020.106784
44. Lednev VN, Grishin MY, Sdvizhenskii ARD, Tretyakov RS, Stavertiy AY, Pershin SM (2019) Sample temperature effect on laser ablation and analytical capabilities of laser induced breakdown spectroscopy. J Anal At Spectrom 34(3):607–615. https://doi.org/10.1039/c8ja00348c
45. Shukla PP, Lawrence J (2010) Fracture toughness modification by using a fibre laser surface treatment of a silicon nitride engineering ceramic. J Mater Sci 45(23):6540–6555. https://doi.org/10.1007/s10853-010-4743-6
46. Wolfram (2020) Thermal Expansion of the Elements. https://periodictable.com/Properties/A/ThermalExpansion.html
47. Schaeffer RD (2012) Fundamentals of laser micromachining. London, UK.
48. Muthuswamy P (2020) Additive manufacturing of tungsten carbide hardmetal parts by selective laser melting (SLM), selective laser sintering (SLS) and binder jet 3D printing (BJ3DP) techniques. Lasers Manuf Mater Process 7(3):338–371. https://doi.org/10.1007/s40516-020-00124-0
49. Khmyrov RS, Safronov VA, Gusarov AV (2017) Synthesis of nanostructured WC-Co hardmetal by selective laser melting. Procedia IUTAM 23(2017):114–119. https://doi.org/10.1016/j.piutam.2017.06.011

50. Zhou X, Liu D, Zhang D, Shen Z, Liu W (2015) Balling phenomena in selective laser melted tungsten. J Mater Process Technol 222(2015):33–42. https://doi.org/10.1016/j.jmatprotec.2015.02.032
51. Khairallah SA, Anderson AT, Rubenchik A, King WE (2016) Laser powder-bed fusion additive manufacturing: physics of complex melt flow and formation mechanisms of pores, spatter, and denudation zones. Acta Mater 108(2016):36–45. https://doi.org/10.1016/j.actamat.2016.02.014
52. Geremia R, Karankis D, Hand DP (2018) The role of laser pulse overlap in ultrafast thin film structuring applications. Appl Phys A Mater Sci Process 124(9):1–8. https://doi.org/10.1007/s00339-018-2045-z